

# UCSF

## UC San Francisco Previously Published Works

### Title

An Atlas of Accessible Chromatin in Advanced Prostate Cancer Reveals the Epigenetic Evolution during Tumor Progression.

### Permalink

<https://escholarship.org/uc/item/42d651dg>

### Journal

Cancer Research, 84(18)

### ISSN

0008-5472

### Authors

Shrestha, Raunak

Chesner, Lisa N

Zhang, Meng

et al.

### Publication Date

2024-09-16

### DOI

10.1158/0008-5472.can-24-0890

Peer reviewed

# 1 **An Atlas of Accessible Chromatin in Advanced Prostate Cancer** 2 **Reveals the Epigenetic Evolution during Tumor Progression**

3 Raunak Shrestha<sup>1,2</sup>, Lisa N. Chesner<sup>1,2</sup>, Meng Zhang<sup>1,2</sup>, Stanley Zhou<sup>3,4</sup>, Adam Foye<sup>1,5</sup>, Arian Lundberg<sup>1,2,6</sup>,  
4 Alana S. Weinstein<sup>1,2</sup>, Martin Sjöström<sup>1,2</sup>, Xiaolin Zhu<sup>1,5</sup>, Thaidy Moreno-Rodriguez<sup>1,7</sup>, Haolong Li<sup>1,2</sup>,  
5 SU2C/PCF West Coast Prostate Cancer Dream Team\*, Joshi J. Alumkal<sup>8</sup>, Rahul Aggarwal<sup>1,5</sup>, Eric J.  
6 Small<sup>1,2,5,7</sup>, Mathieu Lupien<sup>3,4,9,†</sup>, David A. Quigley<sup>1,7,10,†</sup>, Felix Y. Feng<sup>1,2,5,7,†</sup>

7  
8 <sup>1</sup>Helen Diller Family Comprehensive Cancer Center, University of California, San Francisco, San  
9 Francisco, CA, USA

10 <sup>2</sup>Department of Radiation Oncology, University of California, San Francisco, San Francisco, CA, USA

11 <sup>3</sup>Princess Margaret Cancer Centre, University Health Network, Toronto, ON, Canada

12 <sup>4</sup>Department of Medical Biophysics, University of Toronto, Toronto, ON, Canada

13 <sup>5</sup>Division of Hematology and Oncology, Department of Medicine, University of California, San  
14 Francisco, San Francisco, CA, USA

15 <sup>6</sup>The Institute of Cancer Research and The Royal Marsden Hospital, London, UK

16 <sup>7</sup>Department of Urology, University of California, San Francisco, San Francisco, CA, USA

17 <sup>8</sup>Division of Hematology and Oncology, University of Michigan Rogel Cancer Center, Ann Arbor, MI,  
18 USA

19 <sup>9</sup>Ontario Institute for Cancer Research, Toronto, ON, Canada

20 <sup>10</sup>Department of Epidemiology & Biostatistics, University of California, San Francisco, San Francisco,  
21 CA, USA

22 \*A list of members appears in the Supplementary Information

23 †These authors jointly supervised the work  
24

25 **Corresponding Author:** Felix Y. Feng, MD, Department of Radiation Oncology, University of California,  
26 San Francisco, Box 3110, Room 450, 1450 3rd Street, San Francisco, CA 94158. Phone: 415-502-7222; E-  
27 mail: Felix.Feng@ucsf.edu  
28

29 **Running Title:** Accessible Chromatin Landscape of Metastatic Prostate Cancer

## 30 **Conflict of Interest**

31 J.J. Alumkal has consulted for or held advisory roles at Astellas Pharma, Bayer, and Janssen Biotech Inc.  
32 He has received research funding from Aragon Pharmaceuticals Inc., Astellas Pharma, Novartis, Zenith  
33 Epigenetics Ltd., and Gilead Sciences Inc. F.Y. Feng has consulted for Astellas Pharma, Bayer, Blue Earth  
34 Diagnostics, BMS, EMD Serono, Exact Sciences, Foundation Medicine, Janssen Oncology, Myovant,  
35 Roivant, Varian, Tempus and Novartis, and serves on the Scientific Advisory Board for Artera, BlueStar  
36 Genomics, and SerImmune. F.Y. Feng has patent applications with Decipher Biosciences on molecular  
37 signatures in prostate cancer unrelated to this work. F.Y. Feng has a patent application licensed to PFS  
38 Genomics/Exact Sciences. F.Y. Feng has patent applications with Celgene. All other authors declare no  
39 potential conflicts of interest.

40 **Abstract**

41 Metastatic castration-resistant prostate cancer (mCRPC) is a lethal disease that resists therapy targeting  
42 androgen signaling, the primary driver of prostate cancer. mCRPC resists androgen receptor (AR) inhibitors  
43 by amplifying AR signaling or by evolving into therapy-resistant subtypes that do not depend on AR.  
44 Elucidation of the epigenetic underpinnings of these subtypes could provide important insights into the  
45 drivers of therapy resistance. In this study, we produced chromatin accessibility maps linked to the binding  
46 of lineage-specific transcription factors (TF) by performing ATAC sequencing on 70 mCRPC tissue  
47 biopsies integrated with transcriptome and whole genome sequencing. mCRPC had a distinct global  
48 chromatin accessibility profile linked to AR function. Analysis of TF occupancy across accessible  
49 chromatin revealed 203 TFs associated with mCRPC subtypes. Notably, *ZNF263* was identified as a  
50 putative prostate cancer TF with a significant impact on gene activity in the double-negative (AR<sup>-</sup>  
51 neuroendocrine<sup>-</sup>) subtype, potentially activating *MYC* targets. Overall, this analysis of chromatin  
52 accessibility in mCRPC provides valuable insights into epigenetic changes that occur during progression  
53 to mCRPC.

54 **Significance**

55 Integration of a large cohort of transcriptome, whole genome, and ATAC-sequencing characterizes the  
56 chromatin accessibility changes in advanced prostate cancer and identifies therapy-resistant prostate cancer  
57 subtype-specific transcription factors that modulate oncogenic programs.

## 58 **Introduction**

59 Prostate cancer (PCa) is the second leading cause of cancer-related deaths among men (1). Although PCa  
60 is initially responsive to androgen deprivation therapy (ADT), many patients develop resistance and  
61 progress to metastatic castrate-resistant prostate cancer (mCRPC). Targeted systemic therapies with  
62 second-generation AR-signaling inhibitors (ARSIs), such as abiraterone or enzalutamide, prolong survival  
63 and are the standard of care for mCRPC (2–4).

64 Tumors can develop resistance against ADT and/or ARSI through several distinct mechanisms (5). In most  
65 mCRPC, ARSI resistance is achieved through genetic changes that increase AR-signaling (6). Up to 20%  
66 of mCRPCs lose complete *AR* dependence and acquire a new cellular phenotype known as treatment-  
67 emergent small-cell neuroendocrine (NE) prostate cancer (t-SCNC) or neuroendocrine prostate cancer  
68 (NEPC). This AR-NE+ subtype is associated with worse clinical outcomes (7,8). Additional treatment-  
69 associated subtypes have been observed, including a double negative subtype (AR-NE-) that bypasses *AR*  
70 dependence through FGF/MAPK signaling (9,10) and a double positive subtype (AR+NE+) that gains NE  
71 features while maintaining *AR* activity (5). A better understanding of these mCRPC subtypes is foundational  
72 for the development of new approaches to overcome resistance.

73 While *AR* amplification is typical in AR-dependent mCRPCs (11–13) and t-SCNC often harbors *TP53*,  
74 *RBI*, and *PTEN* loss (14), other subtypes have no known characteristic genomic alterations. Emerging  
75 evidence suggests that epigenetic mechanisms are associated with PCa progression and drug resistance  
76 (7,15–17). Specifically, lineage plasticity plays an important role in the development of ARSI resistance  
77 (10,18). It has been increasingly recognized that the complex interplay of epigenetic modifications  
78 including altered chromatin-binding patterns of transcription factors (TFs), such as *AR* and *FOXA1*, regulate  
79 downstream gene activity thereby driving PCa progression (19). Therefore, understanding the chromatin-  
80 binding patterns of TFs that are altered in PCa is crucial for the development of effective therapeutic  
81 strategies.

82 The Assay for Transposase-Accessible Chromatin using sequencing (ATAC-seq) assay has proven to be a  
83 very efficient and general epigenetic assay that yields high-quality chromatin signals from small quantities  
84 of tissue (20,21). ATAC-seq quantifies chromatin accessibility using transposase enzymes that insert  
85 sequencing adapters at accessible chromatin sites. Prior studies (15,21,22) of PCa have mostly used cell  
86 line and organoid models, patient-derived xenografts (PDX), or small numbers of tumor tissue biopsies.  
87 The Cancer Genome Atlas (TCGA) study performed ATAC-seq on multiple cancer types including 26  
88 localized PCa tumors and revealed cancer-type-specific enrichment of TF binding elements in accessible  
89 chromatin regions (21). More recently, using ATAC-seq on CRPC organoids, PDX, and cell lines, Tang et  
90 al. (22) identified four mCRPC subtypes and predicted the key TF of each subtype. To the best of our  
91 knowledge, the characterization of chromatin accessibility in clinical mCRPC biopsy tissue samples using  
92 ATAC-seq has not been conducted to date.

93 Herein, we describe the first-in-field ATAC-seq study conducted in the largest cohort (n=70) of mCRPC  
94 tissue biopsies, to date, from the Stand Up 2 Cancer - Prostate Cancer Foundation West Coast Prostate  
95 Cancer Dream Team (WCDDT) cohort. Using comprehensive integration of ATAC-seq and RNA-seq from  
96 matched tumor samples, we interrogated the changes in chromatin accessibility around regulatory sites to  
97 reveal transcriptional regulation associated with mCRPC subtypes. We used computational approaches to  
98 produce an exhaustive catalog of TFs that are actively occupied in mCRPC and the transcriptional programs

99 they are predicted to regulate. Finally, we exemplified the use of these new data by characterizing *ZNF263*,  
100 a TF previously not associated with PCa biology.

## 101 **Materials and Methods**

### 102 **Patients and samples**

103 Human studies were approved and overseen by the University of California San Francisco Institutional  
104 Review Board. All individuals provided written informed consent to obtain fresh tumor biopsies and to  
105 perform comprehensive molecular profiling of tumor and germline samples. Fresh-frozen metastatic  
106 castration-resistant tissue biopsy samples (n=75) from various anatomic locations representing 69 unique  
107 patients (**Supplementary Figure S1** and **Supplementary Table S1**) were collected through a multi-  
108 institutional image-guided prospective biopsy trial (NCT02432001) and DNA was extracted as previously  
109 described (12,16,17).

### 110 **ATAC-seq library preparation and high-throughput sequencing**

111 The ATAC-seq library preparation was carried out as described in the published method papers by  
112 Buenrostro et al. (20) and Corces et al. (23). Briefly, upon thaw, 30  $\mu$ l of PBS + protease inhibitor was  
113 added onto the slide containing the tissue section and subsequently scraped into a 2 ml tube containing 100  
114  $\mu$ l of cold ATAC-Resuspension Buffer (RSB; 0.1% NP40, 0.1% Tween-20, and 0.01% Digitonin) using  
115 the tip of a scalpel blade. The sample was incubated on ice for 15 minutes intermittently mixing every 5  
116 minutes. After 15 minutes, 1 ml of cold PBS + 0.1% Tween-20 was added into the tube and mixed by  
117 inversion, followed by centrifugation at 500 x g for 10 minutes at 4°C. After centrifugation, the supernatant  
118 was aspirated, avoiding the pellet containing the cell nuclei in the process. 50  $\mu$ l of transposition mix [1X:  
119 25  $\mu$ l of 2X TD buffer (20mM Tris-HCl pH 7.6, 10 mM MgCl<sub>2</sub>, 20% dimethyl formamide), 2.5  $\mu$ l of  
120 transposase, 16.5  $\mu$ l PBS, 0.5  $\mu$ l 1% Digitonin, 0.5  $\mu$ l 10% Tween-20, 5  $\mu$ l water] was added to the nuclei  
121 for resuspension. The reaction was then incubated at 37°C for 30 minutes in a thermomixer with 1000 RPM  
122 mixing. After the transposition reaction, the samples were purified using the Qiagen MinElute PCR  
123 Purification Kit. Upon elution of the DNA, ATAC-seq libraries were prepared. To minimize PCR biases  
124 and duplicates, library preparation was conducted on a real-time qPCR machine, where each sample was  
125 pulled off the machine mid-exponential phase. The resulting ATAC-seq libraries were size-selected with  
126 Ampure XP beads (Beckman Coulter) for 240-360 bp fragments. Upon successful amplification, an aliquot  
127 of the libraries was used for qPCR to calculate the fold enrichment of two accessible chromatin regions  
128 over two inaccessible chromatin regions for quality control (i.e. at least 10-fold enrichment). Samples that  
129 passed quality control were sequenced on the Illumina NovaSeq 6000 sequencing system.

#### 130 POS (Accessible)

131 *GAPDH* (F) 5'-GCCAATCTCAGTCCCTTCCC-3', (R) 5'-TAGTAGCCGGGCCCTACTTT-3'

132 *KAT6B* (F) 5'-GAAGAGGCGGACCCAGCGGT-3', (R) 5'-TTCCTGCCGGTCATCTCGCTT-3'

133

#### 134 NEG (Closed)

135 *SLC22A3* (F) 5'-GGAGAGGGTGGACAGATTGA-3', (R) 5'-TCAGCCTTGCTGCTACAGTG-3'

136 *QML\_93* (F) 5'-CACTGGTTGTCTTTGCAGGA-3', (R) 5'-CCTGGGTCATATTGGGACAC-3'

137

### 138 **ATAC-seq data processing**

139 The ATAC-seq paired-end fastq data was first trimmed to remove the Illumina Nextera adapter sequence  
140 using Cutadapt v2.6 (24) with the “-q 10 -m 20” option (**Supplementary Figure S2**). After adapter

141 trimming, FASTQC v0.11.8 (25) was used to evaluate the sequence trimming as well as overall sequence  
142 quality. Bowtie2 v2.3.5.1 (26) was then used to align the ATAC-seq reads against the Human reference  
143 genome build hg38 using the “--very-sensitive” option. The uniquely mapped reads were obtained in SAM  
144 format. Samtools v1.9 (27) was used to convert SAM to BAM file as well as sort the BAM file. Picard tool  
145 (<https://broadinstitute.github.io/picard>) was then used to flag duplicate reads using the MarkDuplicates  
146 function with the “REMOVE\_DUPLICATES=true” option. The resulting BAM file reads position was  
147 then corrected by a constant offset to the read start (positive-stranded +4 bp, negative-stranded -5 bp) using  
148 deepTools2 v3.3.2 (28) with the “alignmentSieve -ATACshift” option. This resulted in the final aligned,  
149 de-duplicated BAM file that was used in downstream analyses.

150 ATAC-seq peak calling was performed using MACS2 v2.2.5 (29) to obtain narrow peaks with “callpeak -  
151 f BAMPE -g hs -qvalue 0.05 --nomodel -B --keep-dup all --call-summits” option. The resulting peaks that  
152 mapped to the mitochondrial genome or genomic regions listed in the ENCODE hg38 blacklist  
153 (ENCSR636HFF) or peaks that extend beyond the ends of chromosomes were filtered out. The ATAC-seq  
154 peaks were annotated with the nearest gene and genomic region where the peak is located using ChIPseeker  
155 (30) R-package based on hg38 GENCODE v28 annotations. Possible peak annotations are promoter ( $\pm 3$ kb  
156 from TSS), exon, 5'UTR, 3'UTR, intron, and distal intergenic.

### 157 **ATAC-seq quality control**

158 Quality metrics such as Fraction of reads in peak (FRiP) score and fragment length distribution were  
159 calculated as described in Corces et al. (21) and Transcription Start Site (TSS) enrichment score was  
160 calculated using ATACseqQC version 1.18.1 (31). To ensure the quality of our ATAC-seq dataset, we  
161 considered the samples that met the following criteria.

162  $(FRiP\ score > 0.05)\ OR\ (TSS\ Enrich\ score > 8)\ OR\ (ATACseq\ Peak\ counts > 15000)$

163 Five mCRPC samples that failed to satisfy the above criteria were discarded from this study. This resulted  
164 in the final set of 70 samples representing 65 unique patients that were used throughout the study.

### 165 **Consensus ATAC-seq peaks**

166 Non-overlapping unique ATAC-seq narrow peaks regions were obtained from the samples analyzed. Those  
167 non-overlapping unique peak regions present in at least two samples were considered consensus peaks.  
168 Sequencing reads mapped to the consensus peak regions were counted using the “featurecount” function  
169 within Rsubread(32) R-package with the “isPairedEnd=TRUE, countMultiMappingReads=FALSE,  
170 maxFragLength=100, autosort=TRUE” option. The read counts of the consensus peaks were normalized  
171 with the reciprocal of the size factor and variance-stabilized transform method available in the DESeq2(33)  
172 R-package. We note that ATAC-seq peak lengths are highly variable, and so are the lengths of consensus  
173 ATAC-seq peaks. Importantly, ATAC-seq read counts tend to be higher for longer peaks which are not  
174 corrected using DESeq2. To ensure accurate comparisons of the ATAC-seq peaks, throughout the study  
175 comparison is always made between ATAC-seq peaks of the same lengths and never between two peaks of  
176 unequal lengths.

177 The ATAC-seq data (read count profiles) of mCRPC samples from our study were combined with those  
178 from Tang et al.(22). and adjusted for potential batch effects using the “ComBat” function from the “sva”  
179 R-package. Additionally, we attempted to correct potential batch effects in a larger dataset that combined  
180 ATAC-seq profiles of benign prostate, localized PCa, mCRPC adenocarcinoma, and t-SCNC/NEPC from  
181 different datasets. However, this correction was not possible because some sample phenotypes (covariates)  
182 were inseparable from the dataset (batch) they came from.

### 183 **Differential ATAC-seq and RNA-seq analysis**

184 Differential ATAC-seq and RNA-seq analysis for two groups comparison was conducted using the DESeq2  
185 (33) R-package. The normalized read counts of the consensus peaks were used in the case of the ATAC-  
186 seq data. Peaks/genes with Benjamini-Hochberg adjusted  $pvalue \leq 0.01$  and  $|\log_2 folchange| \geq 1$  were  
187 considered statistically significant. For multiple group (3 or more) comparisons of the ATAC-seq dataset,  
188 we used the Kruskal-Wallis test and the peaks with  $pvalue \leq 0.001$  were considered statistically  
189 significant.

### 190 **Pathway enrichment analysis**

191 To test the association of signaling pathways enriched in the accessible chromatin regions (ATAC-seq  
192 peaks), we performed GREAT (34) enrichment analysis using rGREAT R-package. In the case of  
193 enrichment analysis of a list of genes, we used a hypergeometric test-based overrepresentation analysis.  
194 We used the set of signaling pathways genesets in the Reactome, Hallmark pathway, and GO-Biological  
195 Process present in Molecular Signature Database (MSigDB) (35) v7.5.1.

### 196 **Calculation of AR and NE score**

197 The “singscore” (36) R-package was used to calculate AR and NE scores for each mCRPC sample. The  
198 NE score was calculated using the NE genes reported by Beltran et al. (7) and the AR score was calculated  
199 using the gene expression profile of the “HALLMARK\_ANDROGEN\_RESPONSE” geneset from  
200 MSigDB (**Supplementary Table S2**).

### 201 **Transcription factor footprinting**

202 TF footprints were analyzed using Transcription factor Occupancy prediction By Investigation of ATAC-  
203 seq Signal (TOBIAS (37)) version 0.12.11. For TF footprinting analysis, we omitted the step of shifting the  
204 position of aligned reads in the BAM file in our ATAC-seq data processing pipeline (**Supplementary**  
205 **Figure S2**) as this step was already incorporated within the TOBIAS. We called these BAM files and  
206 resulting ATAC-seq peaks, “unshifted”. The input data for TOBIAS were prepared as follows. The  
207 unshifted ATAC-seq BAM files of all samples within a subtype were merged using the “MergeSamFiles”  
208 (Picard) function. A consensus non-overlapping set of unshifted ATAC-seq peaks present in at least two  
209 samples in the subtype was generated. A comprehensive list of 541 unique human TFs was compiled by  
210 combining TFs from the JASPAR (38) CORE database and refined AR binding motifs (Full Site, Half Site,  
211 Lenient Site, and Extended Site) from Wilson et al. (39).

212 First, the insertion bias of the Tn5 transposase was corrected using the “ATACorrect” function taking the  
213 merged unshifted ATAC-seq BAM files and the merged unshifted ATAC-seq peak regions as inputs. The  
214 resulting bigWig files were assigned footprinting scores across all accessible chromatin regions using the  
215 function “ScoreBigwig”. Finally, the scored footprints were matched to the curated list of TF motifs  
216 described above, then differential scores for each motif were determined for each subtype comparison using  
217 the function “BINDetect” with parameters “--motif-pvalue 0.0001; --bound-pvalue 0.001”. TOBIAS  
218 categorizes every predicted TF binding site (for each TF motif) into bound and unbound states based on a  
219 score threshold per subtype compared. The threshold was set at the level of significance (bound p-  
220 value=0.001) of a normal distribution fit to the background distribution of scores.

221 By utilizing this method, we conducted an analysis of differential TF footprinting. This involved comparing  
222 the TF footprints of each mCRPC transcriptional subtype against the others. As a result, we made four  
223 comparisons for each subtype, leading to a total of ten comparisons. From each comparison, the subtype-  
224 associated TF hits were prioritized based on their differential binding score ( $s \geq |0.1|$ ) and associated q-value

225 (top 80% percentile of  $-\log_{10}(q\text{-value})$ ). The pairwise differential TF footprint comparison results between  
226 mCRPC subtypes were further filtered using their gene expression profiles. TFs not expressed (or with  
227 negligible expression level) in relevant subtypes were omitted. These results were visualized in the form of  
228 a circularized heatmap. To generate the heatmap, we computed the TF occupancy phenotype score for each  
229 mCRPC subtype which is determined by the product of the absolute value of the TF binding score and the  
230 absolute value of  $-\log_{10}(q\text{value})$  linked to that specific motif. If a TF is not enriched in a particular subtype,  
231 its score is set to 0.

232 For every mCRPC sample, TF footprinting analysis was also conducted in a single sample mode. For this,  
233 all TOBIAS TF footprinting functions “ATACorrect”, “ScoreBigwig”, and “BINDetect” were executed  
234 using identical parameters to that of the subtype-level analysis except that only one condition (i.e. respective  
235 mCRPC sample) was used in “BINDetect”.

### 236 **Evaluation of the accuracy of TF footprint sites**

237 To assess the accuracy of TOBIAS in predicting TF footprint sites, we compared its predictions with the  
238 TF-binding sites predicted by ChIP-seq. We utilized publicly available ChIP-seq data for *AR*, *FOXAI*, and  
239 *HOXB13* measured in mCRPC from Pomerantz et al. (15). The ChIP-seq TF-binding sites were considered  
240 as the reference or the ground truth. The objective was to determine if TF footprints derived from ATAC-  
241 seq peak regions could accurately capture the ChIP-seq predicted TF-binding regions.

242 Since, the ChIP-seq experiment on mCRPC was limited to *AR*, *FOXAI*, and *HOXB13*, we restricted our TF  
243 footprints evaluation experiment to these three TFs. First, we ran TOBIAS on our ATAC-seq samples using  
244 different “--bound-pvalue” (0.5, 0.1, 0.05, 0.01, 0.005, 0.001, 0.0005, 0.0001) in the “BINDetect” function.  
245 The p-value threshold varies the bound/unbound status assignment for the predicted TF footprint sites. Each  
246 run of TOBIAS using different p-value thresholds resulted in a different set of TF footprint sites. These TF  
247 footprint sites were compared against those observed in the ChIP-seq TF-binding sites. Overlap of at least  
248 1bp between the motif sites from ChIP-seq and ATAC-seq was considered a hit. For each experiment, we  
249 computed the predictions' true positive rate (TPR) and false positive rate (FPR). We then generated receiver  
250 operating characteristic (ROC) curves and calculated the area under the ROC curve (AUC). We repeated  
251 this analysis for every subtype of mCRPC.

### 252 **Reconstruction of TF-target gene regulatory network**

253 The reconstruction of the TF-target gene regulatory network comprises two major steps. (1) Prediction of  
254 TF footprints in accessible chromatin using ATAC-seq (linking TF-peaks as described above) and (2)  
255 associating ATAC-seq peaks that may potentially regulate expression of individual genes (linking peak-  
256 gene). Finally, the TF-peak and peak-gene association results were combined to obtain the TF-gene  
257 association.

258 **Peak-to-gene linking predictions:** We used a correlation-based approach to predict potentially causal links  
259 between ATAC-seq peaks and gene expression. First, the mCRPC RNA-seq gene expression analysis was  
260 restricted to protein-coding genes and filtered out genes not expressed (TPM=0) in more than 25% of all  
261 samples. The ATAC-seq peaks were restricted to those with evidence of TF footprints of at least one out of  
262 541 TFs measured. Our analysis was further restricted to measure cis-interaction (peak-gene association  
263 within the same chromosome). A pairwise Spearman's correlation was measured between every  
264 combination of cis-interacting peak-gene pairs across all mCRPC samples. A permutation experiment was  
265 performed to evaluate the robustness of our peak-to-gene correlation (see below). The majority of the  
266 pairwise peak-gene pairs were random correlations. This warranted an unbiased statistical approach to



267 identify strong correlated or anti-correlated peak-gene pairs. Thus, to identify the most confident set of  
268 peak-gene interaction pairs, we interrogated the enrichment of H3K27ac marks on the peak-gene pairs. We  
269 used three sets of parameters to scrutinize the peak-gene interaction pairs: Spearman's correlation  
270 coefficient ( $R$ ), the p-value of peak-gene interaction pairs through the permutation experiment, and the  
271 distance of the peak to TSS. We used several combinations of values of these three parameters. The peak-  
272 gene interaction pairs generated using the parameters,  $R \geq |0.4|$ ,  $pvalue \leq 0.05$ , and  $distance\ to\ TSS \leq$   
273  $500kb$  had the highest enrichment of H3K27ac peaks. Thus, we used these parameters to prune off weak  
274 peak-gene links.

275 **Permutation experiment:** The gene labels of the RNA-seq gene expression data were randomly permuted,  
276 and the pairwise peak-gene Spearman's correlation was measured across all mCRPC samples. This process  
277 was repeated 1000 different times. Using the density distribution of all permuted Spearman's correlation  
278 coefficients, we calculated p-values for each peak-gene interaction pair.

279 **Reconstruction of the mCRPC subtype-specific regulatory network:** For each mCRPC subtype, we  
280 extracted TF associated with the subtype and genes linked to the subtype associated ATAC-seq peaks. This  
281 resulted in the TF-target gene links associated with the mCRPC subtype.

### 282 **Inferring the effects of ZNF263 binding on transcription of downstream target genes**

283 To investigate how *ZNF263* binding influences the expression of the nearest gene in mCRPC, we evaluated  
284 the changes in gene expression levels that occurred when *ZNF263* was present or absent in the gene's  
285 promoter region. To conduct this analysis, we performed TF footprinting on individual mCRPC samples.  
286 For each gene, we grouped the 70 mCRPC samples based on whether *ZNF263* was present or absent in the  
287 promoter region of the gene. Genes with at least two samples in each group and at least one sample with  
288 expression level  $\log_2\ TPM > 5$  were included for further analysis. Then we performed the Wilcoxon rank  
289 sum test and measured the foldchange in the gene expression levels between the two groups. Genes with  
290 Benjamini-Hochberg adjusted  $pvalue \leq 0.05$  and  $|\log_2\ folchange| \geq 1$  were considered as statistically  
291 significant. The above analysis was also repeated using samples within each subtype (AR+NE-, AR<sub>low</sub>NE-  
292 , and AR-NE-). We note that due to limited samples in AR-NE+, AR-NE-, and AR+NE- subtypes, none of  
293 the genes were statistically significant.

### 294 **Tumor Purity Estimation**

295 Tumor purity of the mCRPC samples used in this study was calculated using PURPLE tool  
296 (<https://github.com/hartwigmedical/hmftools>) based on WGS profiles of the corresponding tumor samples.  
297 In brief, PURPLE combines B-allele frequency (BAF), read depth ratios, somatic variants, and structural  
298 variants to estimate the purity of a tumor sample.

### 299 **Data Availability**

300 The ATAC sequencing data generated in this study are available from the European Genome-Phenome  
301 Archive (EGA) under the accession number EGAS00001006698. The RNA sequencing from the same  
302 tumors is available under the accession numbers EGAD00001008487, EGAD00001008991, and  
303 EGAD00001009065.

304 The RNA-seq data from the WCDT mCRPC cohort was aligned with STAR and quantified at the gene  
305 level for Gencode v28 transcripts as previously described(16). The raw RNA-seq fastq files from PAIR  
306 (40) cohort (GSE115414) and CPCG (41) cohort (EGAD00001004424) were processed and analyzed as  
307 described above. The mRNA expression data of non-diseased tissues was obtained from the GTEx portal  
308 (<https://www.gtexportal.org/>).

309 The publicly available ATAC-seq data used in this study were obtained from Pomerantz et al. (15)  
310 (Sequence Read Archive (SRA) BioProject accession number PRJNA540151), Cejas et al. (42)  
311 (PRJNA691927) and Tang et al. (22) (PRJNA818767). The aligned BAM files from the TCGA localized  
312 PCa ATAC-seq data Corces et al. (21) were obtained from the NIH Genomic Data Commons portal  
313 (<https://portal.gdc.cancer.gov/>). These ATAC-seq data were processed and analyzed using the same ATAC-  
314 seq data processing pipeline described above.

315 mCRPC PDX ChIP-seq data for *AR*, *FOXA1*, *HOXB13*, and H3K27ac were obtained from Pomerantz et al.  
316 (15) Briefly, Raw ChIP-seq data were downloaded from SRA (PRJNA540151). Reads with base quality  
317 scores over 30 across all bases were aligned using bwa-mem v0.7.17 to build hg38. The aligned reads were  
318 deduplicated and peaks were called using MACS2 v.2.2.5, with an FDR threshold of 0.01. Peaks in  
319 ENCODE hg38 blacklist (ENCSR636HFF) were excluded and only peaks that were enriched at least ten-  
320 fold over background were kept for further analysis.

321 The *ZNF263* ChIP-seq peak genomic regions were obtained from Imbeault et al. (43) (GSE78099), Fietze  
322 et al. (44) (GSE19235), and Pope et al. (45) (GSE31477) and *MYC* ChIP-seq peak genomic regions from  
323 Barfeld et al. (46) (GSE73994), See et al. (47) (GSE164777), and Guo et al. (48) (GSE157105). The ChIP-  
324 seq peak regions were uplifted to hg38 before comparing against the TF footprint regions from mCRPC  
325 samples. Further, ChIP-seq profiles of 157 TFs were downloaded from the ChIP-Atlas database (49).

## 326 **Code Availability**

327 Code used in this manuscript is available at [https://github.com/DavidQuigley/WCDT\\_ATAC\\_mCRPC](https://github.com/DavidQuigley/WCDT_ATAC_mCRPC)

## 328 **Results**

329 A prospective multi-institution Institutional Review Board-approved study (NCT02432001) obtained fresh-  
330 frozen core biopsies of metastases from patients with mCRPC as described previously (12,16,17). To create  
331 a rigorous atlas of accessible regulatory DNA elements active in metastatic prostate cancer, we performed  
332 ATAC-seq on 70 mCRPC tissue biopsies obtained from various anatomic locations representing 65 unique  
333 patients (**Supplementary Figure S1** and **Supplementary Table S1**). The ATAC-seq data was processed  
334 using an in-house pipeline (**Methods** and **Supplementary Figure S2**). The sequencing was performed to  
335 remarkably high depth, 204-411 million reads (mean 308 million) (**Supplementary Figure S3a**). This  
336 resulted in an average of 81,215 (range 22,497-157,071) ATAC-seq peaks per sample marking accessible  
337 chromatin regions. We inspected our ATAC-seq dataset using quality control metrics such as the fraction  
338 of reads in peak (FRiP) and transcription start site (TSS) enrichment score. Sample sequencing depth was  
339 not significantly correlated with the number of peaks detected or any quality metrics. The number of peaks  
340 in the sample was significantly correlated with the sample FRiP score (Spearman's correlation coefficient,  
341  $R=0.79$ ,  $p\text{-value}=5.8\times 10^{-16}$ ) (**Supplementary Figure S3b-d**). Tumors with higher estimated purity had  
342 higher FRiP scores ( $R=0.4$ ,  $p\text{-value}=4.4\times 10^{-5}$ ) (**Supplementary Figure S3e**) suggesting that the tumor  
343 content in the tissue sample influenced the ATAC-seq sample quality. ATAC-seq peaks have previously  
344 been reported to occur most frequently in intronic and distal intergenic regions followed by gene promoter  
345 regions, to be enriched at the TSS, and to demonstrate read fragment size periodicity correlated to the  
346 integer multiples of the nucleosome (20,21). Our ATAC-seq data were consistent with those reports  
347 (**Supplementary Figure S3a, S3f-g**). These findings confirmed the high quality of our ATAC-seq data,  
348 consistent with the reports from other groups (20,21).

349 **Chromatin accessibility changes during prostate cancer progression affect stage-specific**  
350 **regulatory elements**

351 To define how chromatin accessibility is altered during prostate cancer progression, we compared the  
352 ATAC-seq profile of our mCRPC samples with publicly available ATAC-seq datasets of benign prostate  
353 (15) (n=4), localized PCa (21) (n=26), and NE PDX models (42) (n=6 with replicates). The ATAC-seq  
354 quality metrics, including the FRiP scores, of our mCRPC samples were comparable to the publicly  
355 available datasets (**Supplementary Figure S4**). We first created a consolidated dataset of ATAC-seq peaks  
356 by merging the complete dataset. This produced a non-overlapping set of 348,799 consensus genomic  
357 regions that were accessible in at least two samples. To test whether this analysis would show systematic  
358 differences in ATAC-seq profiles corresponding to tumor stage, we performed principal component  
359 analysis (PCA) using the normalized read counts of consensus-accessible regions. Our analysis revealed  
360 that mCRPC had distinct chromatin accessibility profiles compared to localized PCa and benign prostate  
361 tissue (**Figure 1a** and **Supplementary Figure S5**). Importantly, among the mCRPC cohort, t-SCNC/NEPC  
362 samples were found to have distinct chromatin accessibility profiles. Corroborating with the prior  
363 observations (15–17), benign prostate and localized PCa had similar chromatin accessibility profiles. A  
364 comparison of the accessible chromatin regions identified that mCRPC had the highest number of genomic  
365 regions with accessible chromatin conformation (**Figure 1b**). This corresponds to our knowledge of the  
366 genome-wide loss of methylation in mCRPC (16,17) and the observation that increased AR expression  
367 results in genome-wide chromatin relaxation (50). Accessible ATAC-seq peaks were extensively shared  
368 across localized PCa, mCRPC, and t-SCNC/NEPC samples (**Figure 1b**) and were enriched in genes  
369 involved in DNA damage repair, apoptosis, and immune system signaling processes (**Supplementary**  
370 **Figure S6**).

371 Chromatin accessibility is known to significantly affect the transcription of nearby genes (21). We noted  
372 there was a robust correlation between the chromatin accessibility of a gene's promoter and the expression  
373 of its corresponding gene (mean Spearman's correlation coefficient,  $R=0.4$ ) (**Supplementary Figure S7a-**  
374 **b**). We found that the differentially expressed genes that were expressed at higher levels were more likely  
375 to have accessible chromatin nearby suggesting that changes in chromatin accessibility can contribute to  
376 differences in gene expression (**Supplementary Figure S7c**). Motivated by this finding, to identify  
377 chromatin variants, the regions of the genome that differ in chromatin accessibility (i.e., differentially  
378 accessible ATAC-seq peaks), between various stages of PCa progression, we performed a differential  
379 accessibility analysis comparing each stage. We further annotated these peaks with the nearest gene and  
380 genomic region where the peak is located (**Methods**). We identified 76,311 (21.9%) peaks that exhibit a  
381 significant change in accessibility in at least one stage (**Figure 1c**). The majority of these peaks were  
382 exclusively detected in mCRPC including the t-SCNC samples (**Figure 1b-c**). These peaks included  
383 promoters of prostate cancer-relevant genes such as *AR*, but most chromatin variants were observed in  
384 introns and distal intergenic regions rather than in promoters (**Figure 1d**). ATAC-seq peaks in distal  
385 intergenic regions of genes such as *AR*, *CHGA*, *DNMT3A*, and *PIK3RI* were exclusively detected in  
386 mCRPC samples. To assess whether chromatin variants were more likely to harbor regulatory DNA, we  
387 intersected these regions with measures of H3K27ac, a histone mark associated with active enhancers, in  
388 mCRPC (15). We observed increased chromatin accessibility of intergenic regions, introns, and promoters  
389 within regions of the H3K27ac signal (**Figure 1e**). We predicted the gene pathways activated by these  
390 chromatin variants using the GREAT enrichment tool (34) and found that the chromatin regions exclusively  
391 accessible in mCRPC-adeno were enriched in the AR signaling pathway, cell migration, and prostate

392 development processes (**Figure 1f**). Accessible chromatin regions in t-SCNC samples were enriched in  
393 neuronal development and differentiation processes. Similarly, chromatin regions accessible in localized  
394 PCa were enriched in lipid biosynthetic and metabolic processes and changes in cytoskeleton organization.  
395 These results imply that the chromatin variants associated with tumor progression potentially deregulate  
396 the oncogenic signaling required for malignant transformation.

### 397 **Chromatin accessibility in mCRPC is associated with subtypes linked to androgen signaling**

398 To investigate the global patterns of chromatin accessibility in mCRPC, we performed unsupervised  
399 hierarchical clustering on ATAC-seq profiles from 70 mCRPC samples. This was achieved by applying  
400 pairwise Spearman's correlation to the normalized read counts of consensus accessible peaks. Our analysis  
401 revealed three distinct clusters of mCRPC samples (**Figure 2a** and **Supplementary Figure S8**). These  
402 clusters were not associated with metastatic tissue sites or alterations of driver genes such as *PTEN*, or *RBI*.  
403 Cluster assignments were, however, correlated with tumor AR-pathway and NE scores assessed by gene  
404 expression signature analysis (**Methods, Figure 2b-c, and Supplementary Table S2**). Tumors in cluster  
405 3 had significantly higher AR scores and lower NE scores (Wilcoxon rank sum test p-value:  $3 \times 10^{-8}$  and  
406  $4 \times 10^{-4}$ ), while tumors in cluster 1 had low AR scores but high NE scores (p-value:  $6.8 \times 10^{-5}$  and  $5 \times 10^{-4}$ ).  
407 Furthermore, leveraging AR and NEPC gene signatures from Labrecque et al. (5), we recently stratified our  
408 mCRPC samples into 5 subtypes (AR+NE, AR<sub>low</sub>NE-, AR+NE+, AR-NE+, and AR-NE-) based on their  
409 RNA-seq gene expression profiles (51). Out of 70 mCRPCs analyzed in this study, 26 tumors were  
410 classified as AR+NE-, 32 tumors as AR<sub>low</sub>NE-, 2 tumors as AR+NE+, 4 tumors as AR-NE+, and 6 tumors  
411 as AR-NE- (**Supplementary Table S1**). Cluster 1 was associated with the AR-NE+ subtype (Fisher's Exact  
412 Test p-value=0.003) whereas cluster 3 was associated with AR+NE- subtype (p-value=0.005). Cluster 2  
413 had mixed sample phenotypes, with almost 58% of the samples in the group associated with AR<sub>low</sub>NE-  
414 subtypes and 25% of the samples associated with AR+NE- subtype. We further observed that clusters 2  
415 and 3 each contained two sub-clusters designated as 2A and 2B, and 3A and 3B respectively. These sub-  
416 clusters were primarily distinguished by variations at the tissue level. Notably, both sub-clusters 2B (p-  
417 value=0.002) and 3A (p-value=0.002) were enriched with bone metastatic tissue biopsies. A recent study  
418 of chromatin availability in cell lines and organoid models by Tang et al. (22) reported the existence of four  
419 ATAC-seq subtypes of CRPC: CRPC-AR, CRPC-NE, CRPC-WNT, and stem cell-like (CRPC-SCL)  
420 subtypes. To compare these subtypes with our cohort of mCRPC samples, we analyzed ATAC-seq data  
421 from both studies together. Unsupervised hierarchical clustering of ATAC-seq profiles showed that the  
422 majority of samples in CRPC-AR and AR+NE- subtypes were a part of the same cluster (**Supplementary**  
423 **Figure S9**). Similarly, samples in CRPC-NE and CRPC-WNT subtypes clustered together with the AR-  
424 NE+ subtype. Samples in the CRPC-SCL subtype were clustered with AR<sub>low</sub>NE- and AR-NE- subtypes.  
425 These results indicate that the chromatin accessibility in our mCRPC data was linked most strongly with  
426 mCRPC transcriptional subtypes.

### 427 **mCRPC transcriptional subtypes are associated with chromatin variants of prostate cancer** 428 **signaling pathways**

429 After establishing that androgen signaling was significantly associated with chromatin accessibility status  
430 genome-wide, we performed a supervised analysis to identify chromatin loci whose accessibility status was  
431 correlated with the five mCRPC transcriptional subtypes from Labrecque et al. (5). This analysis was  
432 motivated by our observation that chromatin accessibility proximal to the genes that defined mCRPC  
433 transcriptional subtype signatures were correlated with gene expression of the corresponding gene

434 **(Supplementary Figure S10)**. Moreover, there was no significant difference between the numbers of peaks  
435 and FRiP score among the mCRPC transcriptional subtypes **(Supplementary Figure S11)**.

436 We, therefore, tested for differential chromatin accessibility across the five mCRPC subtypes. This analysis  
437 identified 6704 ATAC-seq peaks with significant differences in accessibility across all samples in each of  
438 the subtypes **(Supplementary Table S3)**. AR+NE- tumors most frequently harbored increased  
439 accessibility, followed by AR<sub>low</sub>NE- tumors **(Figure 3a)**, in PCa-associated genes such as *AR*, *KLK3*,  
440 *FOXA1*, *NKX3-1*, *SPOP*, *ZBTB16*, and *NCOA2*. Similarly, regions around several epigenetic drivers of  
441 prostate cancer such as *ARID1A*, *SMARCA1*, *KMT2D*, and *KDM6A* were more accessible in AR+NE- and  
442 AR<sub>low</sub>NE- tumors compared to the remaining subtypes. Interestingly, most chromatin variants between the  
443 mCRPC subtypes were annotated distal to the TSSs (i.e. distal intergenic peaks); about 75% of chromatin  
444 variants were located more than 3kb from TSS **(Supplementary Figure S12a)**. These regions may  
445 represent enhancer regions active in specific subtypes of the disease. One such example was a distal  
446 accessible region upstream of the *AR* that we and others have previously identified as a driver of ADT and  
447 ARSI resistance in AR-positive disease (12,13). We additionally identified chromatin variants in distal  
448 regions near *NKX3-1* in AR+NE- and AR<sub>low</sub>NE- subtypes, and *GPR37LI* in AR+NE- subtype as compared  
449 to the remaining subtypes **(Figure 3b)**. *GPR37LI* encodes for a G protein-coupled receptor protein almost  
450 exclusively expressed in the nervous system, and studies in murine models have suggested it to have a  
451 neuroprotective function (52). *AR* and *NKX3-1* mRNA were expressed in AR+NE- and AR<sub>low</sub>NE- subtypes  
452 and *GPR37LI* mRNA was highly expressed in AR-NE+ subtypes **(Supplementary Figure S12b-d)**.  
453 Moreover, these chromatin variants in *AR*, *NKX3-1*, and *GPR37LI* were correlated with their corresponding  
454 gene expression **(Supplementary Figure S12e-g)**.

455 To gain insight into the functional role of accessible chromatin, we extracted the chromatin variants across  
456 all mCRPC transcriptional subtypes that mapped to the promoter, intron, and distal intergenic regions  
457 **(Figure 3c)**. Chromatin variants in the promoter, intron, and distal intergenic regions were enriched for the  
458 Hallmark Androgen Response pathway **(Figure 3d-f)**. Chromatin regions mapped to intron and intergenic  
459 were also enriched in oncogenic and proliferative signaling pathways. This underscores the functional  
460 importance of intronic and distal intergenic chromatin variants in potentially modulating the epigenetic  
461 landscape of mCRPC transcriptional subtypes.

## 462 **mCRPC transcriptional subtypes are defined by DNA accessibility-guided patterns of** 463 **transcription factor regulation**

464 Following our observation that the regulatory elements are enriched in the accessible chromatin region in  
465 mCRPC, we built a comprehensive catalog of transcription factors (TF) occupancy across mCRPC  
466 transcriptional subtypes. TF binding to chromatin prevents Tn5 cleavage within the binding site and  
467 generates depletion in ATAC-seq coverage known as “TF footprints” (53). We interrogated TF footprint  
468 signals in the accessible chromatin of mCRPCs using the TOBIAS (37) software tool. First, to evaluate the  
469 reliability of the predicted TF footprints, we compared the *AR*, *FOXA1*, and *HOXB13* footprints predicted  
470 in our mCRPC samples against the respective ChIP-seq binding sites observed in mCRPC PDX samples  
471 obtained from Pomerantz et al. (15) **(Methods)**. Our analysis found that TOBIAS-predicted TF footprint  
472 sites were correlated to experimentally observed ChIP-seq binding sites **(Supplementary Figure S13a-f)**.  
473 For each TF, TOBIAS classifies every predicted TF binding site as a bound or unbound state based on a  
474 user-defined footprint score threshold **(Methods)**. The bound TF footprint sites were observed to have a  
475 depleted ATAC-seq accessibility signal as compared to the unbound sites **(Figure 4a-b)**. Moreover, a

476 significant proportion (82-96%) of the predicted TF-bound footprint sites were found to coincide with the  
477 regions identified by ChIP-seq peaks as compared to the unbound sites (**Supplementary Figure S13g-i**).  
478 This suggests that our predictions of TF footprints are strong and reliable.

479 Next, we performed an unbiased genome-wide active TF occupancy analysis using 541 human TFs  
480 (**Supplementary Figure S14**) from the JASPAR (54) database and examined their association with  
481 different mCRPC transcriptional subtypes. We performed an unbiased differential TF footprint occupancy  
482 analysis comparing each mCRPC transcriptional subtype to the other (**Figure 4c-d** and **Supplementary**  
483 **Figure S15**). Subtype-associated TF hits were prioritized based on their differential binding score and  
484 associated probability score (**Methods** and **Supplementary Table S4**). For example, *AR*, *FOXA1*,  
485 *HOXB13*, and *NR3C1* were identified to have differential TF footprint occupancy in AR+NE- compared to  
486 AR-NE+ or AR-NE- subtypes (**Figure 4c-d** and **Supplementary Table S4**). Similarly, TFs such as *ASCL1*,  
487 *NEUROD1*, *SNAI2*, *ID4*, and *NKX3-2* were identified to have differential TF footprint occupancy in AR-  
488 NE+ compared to AR+NE- subtype. AR-NE- tumors were enriched for high TF footprint occupancy of  
489 *SP1*, *SP2*, *ZNF263*, and *KLF5* (**Figure 4d**).

490 We aggregated the results of significantly differential occupied TFs from all ten pairwise comparisons  
491 between the mCRPC subtypes and identified 203 TFs enriched in distinct mCRPC subtypes (**Figure 4e** and  
492 **Supplementary Table S5**). To further validate our predictions through computational analysis, we  
493 compared our predicted TF footprints to publicly available data on binding sites for 120 TFs obtained using  
494 ChIP-seq (**Supplementary Figure S16**). Our analysis revealed that for 94 of these factors, at least 25% of  
495 our predicted footprint locations overlapped with the ChIP-seq binding sites. For TFs known to be  
496 associated with prostate cancer, such as *FOXA1*, *AR*, *ERG*, *HOXB13*, *NR3C1*, *ASCL1*, and *GATA2*, the  
497 overlap between our predicted footprints and the ChIP-seq data was even greater, with over 80%  
498 concordance.

499 We observed that TFs such as *AR*, *FOXA1*, *HOXB13*, *GATA2*, *SP1*, *SP2*, and *KLF5* were enriched in  
500 multiple subtypes. Eighty-four TFs were associated with both AR+NE- and AR<sub>low</sub>NE- subtypes indicating  
501 similarity in gene transcription regulation between these two subtypes. About 80% (20 of 25) of AR-NE-  
502 TFs were also associated with the AR<sub>low</sub>NE- subtype corroborating previous (5) observations of  
503 transcriptomic similarity between AR<sub>low</sub>NE- and AR-NE-. Interestingly, each subtype of mCRPC shows a  
504 distinct affinity towards certain subtype-specific TFs. For example, a large set of 49 TFs, comprising  
505 *ASCL1*, *NEUROD1*, *NKX3-2*, and *POU3F2* was found to be exclusively associated with the AR-NE+  
506 subtype. *ASCL1* is a pro-neural TF that acts as a driver of the neuronal transcriptional program to support  
507 treatment resistance in the AR-NE+ subtype (42,55). Similarly, *POU3F2* is a neural TF that is directly  
508 suppressed by *AR* and mediates NE differentiation and treatment resistance in the AR-NE+ subtype (56).  
509 *NEUROD1* is a neuronal TF associated with neuronal development in both NEPC and small-cell lung  
510 cancer (SCLC) (42). Our results provide a unique opportunity to comprehensively interrogate several TFs  
511 associated with mCRPCs.

512 Knowing where TFs bind on the genome is important because it can provide valuable insights into the gene  
513 expression regulatory mechanisms. Therefore, we examined the locations of all predicted TF footprints in  
514 the genome. We observed that in all TFs, the footprints were identified in both the promoter and distal to  
515 the promoter regions of the nearest gene (**Supplementary Figure S17**). In 72% (147 of 203) of the TFs,  
516 the majority of the footprints were observed at a distance of more than 3kb from the nearest gene, whereas,  
517 in the remaining 28% (56 of 203) of the TFs, the footprints were observed within the promoter region (i.e.,  
518 TSS±3kb). Intriguingly, we found that all TFs associated with AR-NE- were preferentially localized in the

519 promoter region. This finding was corroborated by analyzing independent publicly available ChIP-seq  
520 profiles of TFs associated with the AR-NE- subtype (**Supplementary Figure S18**). Since the promoters in  
521 humans are enriched for the CpG dinucleotide, TFs such as *SPI1*, *NRF1*, *ETS*, and many C2H2 zinc finger  
522 proteins including KLF-family proteins and *ZNF263* are known to preferentially bind proximal promoter  
523 DNA sequences (44,57). Thus, ATAC-seq-based TF footprinting allows us to examine the preferred  
524 binding regions of a vast number of TFs.

## 525 **Identification of the influential transcription factors in mCRPC transcriptional subtypes**

526 To identify the functional impact of mCRPC subtype-specific TF binding patterns, we constructed unbiased  
527 gene expression networks associated with each TF binding event. We integrated ATAC-seq and matched  
528 RNA-seq data from our mCRPC cohort to comprehensively identify correlated or anti-correlated genome-  
529 wide cis-interacting peak-gene pairs (**Methods** and **Supplementary Figure S19**). We identified a set of  
530 37,865 robust peak-gene pairs (36,616 correlated and 1,249 anti-correlated pairs) consisting of 23,089  
531 unique peaks and 7,710 unique genes (**Supplementary Figure S20a-c**). On average, 1.64 (min=1, max=29)  
532 genes were associated with a peak (**Supplementary Figure S20d**). Approximately 98% of peaks were  
533 correlated with 5 genes or less and 66% of peaks were associated with only 1 gene. Similarly, on average,  
534 5 (min=1, max=108) peaks were associated with a gene (**Supplementary Figure S20e**). About 76% of  
535 genes were associated with at most 5 peaks and 35% of genes were associated with only 1 peak. Most  
536 correlated peaks were proximal to the TSS region of a gene, as compared to its distal region  
537 (**Supplementary Figure S20f**). These mCRPC TF network characteristics are consistent with the results  
538 obtained from TF networks derived from ATAC-seq in various types of cancer(21,22). We further  
539 integrated the TF footprint sites identified in the accessible peak to the genes correlated with the peak to  
540 construct a TF-target gene regulatory network and identify the target genes of TFs. Restricting our analysis  
541 to the 203 mCRPC-associated TFs, the regulatory network represented 22,608 unique peaks and 7,632  
542 unique genes. Based on the ATAC-seq peaks observed in individual mCRPC subtypes and the associated  
543 TFs, we derived the mCRPC subtype-specific regulatory network.

544 Taking advantage of these dense regulatory networks, we assessed if we could identify influential TFs  
545 potentially regulating the transcriptional programs and driving the mCRPC subtypes. We hypothesized that  
546 highly influential TFs regulate the transcriptional activity of a large fraction of the downstream target genes.  
547 Thus, we computed the node degree of the TFs in mCRPC subtype-specific regulatory networks (**Figure 5**  
548 and **Supplementary Table S6**). We found that several of our top-influential TF hits were well-established  
549 drivers of PCa. *FOXA1* and several FOX-family TFs including *FOXC2*, *AR*, *HOXB13*, *GRHL2*, and *SRY*  
550 were predicted as the top influential TFs in the AR+NE- subtype. *FOXA1* and *AR* are well-established as  
551 drivers of mCRPC (11,12,16,17,58,59). The top influential TFs in the AR-NE+ subtype such as *ASCL1*  
552 (42,55), *NEUROD1* (42), *ZEB1* (60), *TCF4* (61), and *SNAI2* (62) are known to promote neuroendocrine  
553 differentiation in PCa. The AR+NE+ subtype was enriched with influential TFs found in both AR+ and  
554 NE+ subtypes. The Stripe family (63) of TFs including *SPI1*, *SP2*, and *KLF5* (64) were predicted to drive  
555 both AR<sub>low</sub>NE- and AR-NE- subtypes. This suggests that our analysis nominated consistent TFs hits  
556 associated with PCa. Furthermore, this analysis identified several influential TFs that were not previously  
557 linked to PCa, including *ZNF263* and *RREB1* in AR-NE- subtype, *ZNF384* and *CDX1* in AR+NE- subtype,  
558 and *BACH2* and *ZBTB18* in the AR-NE+ subtype. To explore the regulatory impact of the hits identified  
559 through TF footprinting analysis on their target genes, we opted to investigate *ZNF263* since it has not been  
560 studied in the context of mCRPC.

561 **ZNF263 regulates the MYC signaling pathway in mCRPC**

562 *ZNF263* has been implicated in modulating oncogenic signaling in cancers. For example, *ZNF263* is the  
563 most significant TF bound to the endoplasmic reticulum stress-specific super-enhancer and is highly  
564 expressed in hepatocellular carcinoma (HCC) (65). *ZNF263* knockdown in HCC cell lines leads to reduced  
565 proliferation, apoptosis resistance, and chemoresistance (65). *ZNF263* enhances *EGFR* signaling and the  
566 progression of glioblastoma (66). Despite having a KRAB domain that typically facilitates transcriptional  
567 repression, *ZNF263* can exert both positive and negative impacts on the transcriptional regulation of the  
568 genes it targets (44). However, *ZNF263* has not been studied in the context of prostate cancer.

569 First, to establish the relevance of *ZNF263* in prostate cancer, we interrogated its mRNA expression in  
570 several publicly available datasets. Our analysis of gene expression profiles of non-diseased tissues  
571 indicated that *ZNF263* is highly expressed in prostate tissues (**Supplementary Figure 21a**). Moreover, we  
572 found elevated expression levels of *ZNF263* in mCRPC as compared to both benign prostate and localized  
573 PCa tissue (**Supplementary Figure 21b-c**). Notably, *ZNF263* was expressed in all mCRPC subtypes and  
574 there was no difference in expression levels between the subtypes (**Supplementary Figure 21d**). Next, to  
575 inspect the reproducibility of our predicted *ZNF263* footprint sites, we compared predicted binding sites in  
576 mCRPC to previously published *ZNF263* ChIP-seq profiles measured on human embryonic stem cells and  
577 erythroblast cells. We hypothesized that although some *ZNF263* binding sites would be unique to mCRPC,  
578 many binding sites would be invariant among cell types, and demonstrating non-random enrichment for  
579 experimentally identified binding sites would support the validity of our computational analysis. Indeed,  
580 we found that 6-16% of *ZNF263* bound footprint sites were also observed in the ChIP-seq peaks  
581 (hypergeometric test p-value <  $2.2 \times 10^{-16}$ ) (**Supplementary Figure S22a**). Importantly, sites where we  
582 predicted TF binding in mCRPC had a greater degree of overlap with the ChIP-seq peaks than sites  
583 predicted to be unbound in mCRPC, supporting the robustness of our footprint predictions.

584 To identify targets of *ZNF263* transcriptional regulation in mCRPC, we assessed variation in gene  
585 expression levels in the presence or absence of *ZNF263* binding. As described in the previous section, since  
586 *ZNF263* has a strong affinity for binding to the promoter region (**Supplementary Figure S17 and S18**),  
587 we focused our analysis on *ZNF263* footprints identified in this region. For each gene, we grouped the  
588 mCRPC samples based on whether *ZNF263* was present or absent in the promoter region of the gene. Then  
589 we measured the foldchange in the gene expression levels between the two groups. A significant increase  
590 in gene expression levels was observed for most genes when *ZNF263* was bound to their promoter region  
591 (**Figure 6a**). We conducted an unbiased enrichment analysis to identify common functions of genes whose  
592 expression increased when *ZNF263* was bound and identified enrichment in the MYC signaling pathways  
593 (**Supplementary Figure S22b**). Conducting the same analysis on individual mCRPC transcriptional  
594 subtypes produced comparable findings to the analysis that included all samples (**Supplementary Figure**  
595 **S22c-d**). We observed that *ZNF263* footprints were prevalent in all mCRPC subtypes. However, when  
596 compared to other subtypes, the AR-NE- subtype exhibited a higher occupancy of *ZNF263* footprints  
597 (**Supplementary Figure S22e**). Interestingly, the target genes of *ZNF263* including *MYC* targets were  
598 expressed in AR-NE- subtype as well as many other samples from different other mCRPC subtypes  
599 (**Supplementary Figure S23**). These results suggest that *ZNF263* potentially acts as an activator of gene  
600 expression in all mCRPC subtypes.



601 Next, to further strengthen our findings, we tested the enrichment of *ZNF263* target genes obtained using  
602 TF network analysis. Indeed, *MYC* signaling was the top-most enriched pathway followed by several other  
603 proliferation and oncogenic signaling pathways (**Figure 6b** and **Supplementary Figure S24a**). Conducting  
604 the same TF network analysis for *MYC* revealed that the genes predicted to be up-regulated when *MYC* is  
605 bound significantly overlap with genes targeted by *ZNF263* (**Figure 6c**). We also investigated genes that  
606 are regulated by both *ZNF263* and *MYC*. Interestingly, the top enriched pathways were those involved in  
607 *MYC* and androgen response signaling (**Supplementary Figure S24b**). The evidence presented above  
608 suggests that *ZNF263* potentially influences the activity of *MYC* target genes.

609 Further, we inspected the *ZNF263* footprints and their association with that of *MYC*. Despite having a  
610 different motif sequence than that of *MYC* (**Supplementary Figure S24c**), approximately 0.35% of all  
611 *ZNF263* footprint sites overlap with the footprints of *MYC* and 2.75% of all *MYC* footprints overlap with  
612 that of *ZNF263* (**Figure 6d**). We further excluded these overlapping footprint regions and measured the  
613 distance between the remaining *ZNF263* and its nearest *MYC* binding site. We found *MYC*-occupied regions  
614 near *ZNF263* binding sites more often in the AR-NE- subtype as compared to the rest of the mCRPC  
615 transcriptional subtypes (**Supplementary Figure S24d**). Furthermore, we evaluated if *ZNF263* footprints  
616 predicted using ATAC-seq overlap with *MYC* ChIP-seq predicted binding sites. For this, we leveraged  
617 publicly available *MYC* ChIP-seq profiles measured on different prostate cancer and osteosarcoma cell  
618 lines. We found that about 15-20% of *ZNF263* bound footprint sites overlap with the *MYC* ChIP-seq  
619 predicted binding sites (hypergeometric test p-value  $< 2.2 \times 10^{-16}$ ) (**Supplementary Figure S24e**). Thus,  
620 implying that *MYC* binds near the binding sites of *ZNF263*.

621 We next tested the hypothesis that *ZNF263* is a co-activator of *MYC* transcriptional targets in mCRPC.  
622 *ZNF263* was predicted to bind more gene promoter sites than *MYC* in AR+ and AR- subtypes  
623 (**Supplementary Figure S24f**). We tested whether *MYC* targets were differentially expressed when both  
624 *ZNF263* and *MYC* were bound in the promoter region, in comparison with *ZNF263* alone or neither protein.  
625 Supporting our hypothesis, the presence of *ZNF263* binding increased the expression level of these genes  
626 (**Figure 6e**), and the concomitant binding of *ZNF263* and *MYC* further increased the expression level of  
627 *MYC* target genes (**Figure 6f**). These observations are consistent with a model that *ZNF263* collaborates  
628 with *MYC* to activate *MYC* targets in mCRPC.

## 629 Discussion

630 The prolonged usage of ADT and/or ARSI in advanced prostate cancer leads to the emergence of a diverse  
631 spectrum of mCRPC subtypes. While there are emerging genomic and transcriptomic distinctions between  
632 the mCRPC subtypes, information regarding the variations in the epigenomic regulatory landscape between  
633 the subtypes is scarce. In this study, we present a comprehensive characterization of the chromatin  
634 accessibility of mCRPC using integrated analysis of ATAC-seq and RNA-seq from matched samples.  
635 Earlier studies (15,21,22) on mCRPC predominantly depended on cell lines, organoids, PDXs, or a limited  
636 number of mCRPC tissue biopsies. To date, our study represents the largest group of mCRPC tissue  
637 biopsies that have been characterized using ATAC-seq. Here, we show that chromatin accessibility  
638 increases during PCa progression to mCRPC. Importantly, we found mCRPC to have unique chromatin  
639 accessibility profiles compared to localized PCa and benign prostate. AR signaling is the major driver of  
640 mCRPC(11–13,16,17) and our investigation indicated that the functional activity of AR predominantly  
641 governs the chromatin accessibility patterns in mCRPC. The ATAC-seq profile of our mCRPC cohort

642 closely recapitulates the chromatin accessibility heterogeneity in the advanced PCa patient population.  
643 Furthermore, the subtypes Tang et al. (22) identified through the analysis of ATAC-seq profiles in CRPC  
644 cell lines, organoid, and PDX models were similar to the mCRPC subtypes reported in our study.  
645 Particularly noteworthy was the finding that the CRPC-WNT and CRPC-SCL subtypes predominantly  
646 represented AR- subtypes.

647 This study evaluated differences in chromatin accessibility across 5 mCRPC subtypes. Among these  
648 subtypes, AR+NE- and AR-NE+ (t-SCNC/NEPC) subtypes have been extensively studied and well  
649 characterized, while AR<sub>low</sub>NE-, AR+NE+, and AR-NE- subtypes remain relatively less explored. By  
650 integrating ATAC-seq and RNA-seq of matched tumors, we established a correlation between the  
651 accessibility of a regulatory element to the expression levels of predicted target genes. We then conducted  
652 a thorough analysis of TF occupancy signals across the entire accessible genomic regions, leading us to  
653 identify 203 TFs that are linked to specific mCRPC subtypes. Some TFs are uniquely enriched in a certain  
654 mCRPC subtype whereas others are common to multiple subtypes. We found that a variety of TFs were  
655 associated with the t-SCNC phenotype. Furthermore, we found that AR<sub>low</sub>NE- and AR-NE- have many  
656 common TFs, which further supports the previous (5) findings suggesting that these subtypes share common  
657 signaling pathways. We observed the presence of numerous TFs associated with AR+NE- in both AR<sub>low</sub>NE-  
658 and AR+NE+ subtypes. Additionally, the AR+NE+ subtype displayed enrichment of several NE-related  
659 TFs. Thus, our analysis suggests that AR<sub>low</sub>NE-, AR+NE+, and AR-NE- subtypes might potentially be an  
660 intermediate phenotype between the more extreme AR+NE- and AR-NE+ subtypes. A recent study (5) has  
661 reported the existence of multiple mCRPC subtypes within the same metastatic site of a patient supporting  
662 mCRPC disease continuum hypothesis. These diverse spectra of mCRPC subtypes are believed to emerge  
663 from intertumoral heterogeneity and treatment-induced selective pressures that can change the phenotypic  
664 and molecular landscapes of mCRPC (5). This mandates a detailed study interrogating the molecular  
665 mechanisms driving these rare intermediate mCRPC subtypes and their clinical outcome for better  
666 management of mCRPC.

667 Our analysis identified both established mCRPC-associated TFs as well as TFs that are relatively under-  
668 studied in the context of PCa. Our interest in investigating *ZNF263* was driven by several studies linking  
669 the altered activity of *ZNF263* to oncogenic processes and chemotherapy resistance in different cancers  
670 (65,66). To the best of our knowledge, the role of *ZNF263* in prostate cancer has not been studied to date.  
671 Here, we demonstrate that *ZNF263* has a considerable influence on modulating the gene expression in  
672 mCRPC and may collaborate with *MYC* in these tumors. Thus, the integration of ATAC-seq and RNA-seq  
673 data in our work demonstrates the ability to investigate the effects of TF binding on the activity of their  
674 downstream target genes.

675 Our comprehension of gene expression regulation relies heavily on understanding TF binding to regulatory  
676 elements (21). Traditionally, ChIP-seq has been the standard method for identifying TF binding sites, but  
677 more recently, ATAC-seq has emerged as a promising alternative (20,67). Unlike ChIP-seq, which requires  
678 specific antibodies targeting individual TFs, ATAC-seq enables comprehensive genome-wide profiling of  
679 footprints of all known TFs within the accessible chromatin regions. Thus, ATAC-seq TF footprint  
680 prediction holds promise as a method to screen the genome-wide binding of an extensive range of TFs in a  
681 single analysis framework to gain a comprehensive understanding of gene regulation and further reconstruct  
682 subtype-specific regulatory networks.

683 Transcription factors are alluring as therapeutic targets because they are master regulators of large gene  
684 networks that affect disease outcomes. Although TFs are conventionally considered difficult-to-drug  
685 proteins, promising technologies such as PROTAC (68) have enabled the targeted degradation of desired  
686 proteins, including TFs. Direct (PROTAC) or indirect inhibition of several TFs is currently being  
687 investigated in clinical trials (69). ATAC-seq TF footprinting can aid in the identification of potential  
688 therapeutic targets by providing information on the regulatory regions of genes that are accessible to TF  
689 binding.

690 In summary, this study characterizes the changes in chromatin accessibility in advanced PCa. Our results  
691 illustrate the importance of studying chromatin shifts at regulatory regions to determine TFs actively  
692 occupied in the region, and how they modulate transcriptional programs associated with oncogenic and  
693 tumor-suppressive functions. Overall, our findings provide valuable insights into epigenetic changes that  
694 occur during mCRPC progression.

## 695 **Authors' Contributions**

696 **R. Shrestha:** Conceptualization, Data curation, Formal Analysis, Investigation, Methodology, Software,  
697 Visualization, Writing – original draft, Writing – review & editing. **L.N. Chesner:** Data curation,  
698 Methodology, Writing – review & editing. **M. Zhang:** Data curation, Methodology, Software, Writing –  
699 review & editing. **S. Zhou:** Methodology, Writing – review & editing. **A. Foye:** Data curation,  
700 Methodology, Project administration, Resources, Writing – review & editing. **A. Lundberg:** Data curation,  
701 Methodology, Software, Writing – review & editing. **A.S. Weinstein:** Data curation, Methodology,  
702 Software, Writing – review & editing. **M. Sjöström:** Data curation, Methodology, Software, Writing –  
703 review & editing. **X. Zhu:** Data curation, Methodology, Software, Writing – review & editing. **T. Moreno-**  
704 **Rodriguez:** Data curation, Methodology, Software, Writing – review & editing. **H. Li:** Data curation,  
705 Methodology, Writing – review & editing. **SU2C/PCF West Coast Prostate Cancer Dream Team:**  
706 Resources, Writing – review & editing. **J.J. Alumkal:** Resources, Writing – review & editing. **R.**  
707 **Aggarwal:** Resources, Writing – review & editing. **E.J. Small:** Funding acquisition, Resources, Writing –  
708 review & editing. **M. Lupien:** Funding acquisition, Investigation, Methodology, Supervision, Writing –  
709 review & editing. **D.A. Quigley:** Conceptualization, Data curation, Funding acquisition, Investigation,  
710 Methodology, Project administration, Software, Supervision, Writing – review & editing. **F.Y. Feng:**  
711 Conceptualization, Funding acquisition, Investigation, Methodology, Project administration, Supervision,  
712 Writing – review & editing.

## 713 **Acknowledgments**

714 The authors thank the patients who selflessly contributed samples to this study, without whom this research  
715 would not have been possible. This research was supported by a Stand Up To Cancer-Prostate Cancer  
716 Foundation Prostate Cancer Dream Team Award (SU2C-AACR-DT0812 to E.J.S.) and by the Movember  
717 Foundation. This research grant was administered by the American Association for Cancer Research, the  
718 scientific partner of SU2C. R. Shrestha, M. Sjöström, X. Zhu, and H. Li were supported by Prostate Cancer  
719 Foundation (PCF) Young Investigator Award. L.N. Chesner was supported by the PCF Young Investigator  
720 Award and the Department of Defense Early Investigator Award (W81XWH2110046). M. Lupien was  
721 funded by the Canadian Institute of Health Research (CIHR) (FRN-153234 and 168933), the Ontario  
722 Institute for Cancer Research (OICR) Investigator Award through funding provided by the Government of  
723 Ontario, and the Princess Margaret Cancer Foundation. D.A. Quigley was funded by a Young Investigator

724 and Challenge awards from the PCF and by the UCSF Benioff Initiative for Prostate Cancer Research. F.Y.  
725 Feng was funded by PCF Challenge Awards. Additional funding was provided by a UCSF Benioff Initiative  
726 for Prostate Cancer Research award. F.Y. Feng was supported by the National Institutes of Health  
727 (NIH)/National Cancer Institute (NCI) 1R01CA230516-01. F.Y. Feng was supported by NIH/NCI  
728 1R01CA227025 and PCF 17CHAL06. F.Y. Feng was supported by NIH P50CA186786. J.J. Alumkal was  
729 supported by NCI R01 CA251245, NCI P50 CA097186, NCI P50 CA186786, NCI P50 CA186786-07S1,  
730 Joint Institute for Translational and Clinical Research, and a PCF Challenge Award. The list of members  
731 in the SU2C/PCF West Coast Prostate Cancer Dream Team is provided in the Supplementary Appendix.

732 **References**

- 733 1. Siegel RL, Miller KD, Fuchs HE, Jemal A. Cancer statistics, 2022. *CA Cancer J Clin* [Internet].  
734 American Cancer Society; 2022 [cited 2022 Dec 23];72:7–33. Available from:  
735 <https://onlinelibrary.wiley.com/doi/full/10.3322/caac.21708>
- 736 2. de Bono JS, Logothetis CJ, Molina A, Fizazi K, North S, Chu L, et al. Abiraterone and Increased  
737 Survival in Metastatic Prostate Cancer. *n engl j med*. 2011.
- 738 3. Scher HI, Fizazi K, Saad F, Taplin M-E, Sternberg CN, Miller K, et al. Increased Survival with  
739 Enzalutamide in Prostate Cancer after Chemotherapy. *New England Journal of Medicine*. *New*  
740 *England Journal of Medicine (NEJM/MMS)*; 2012;367:1187–97.
- 741 4. Ryan CJ, Smith MR, de Bono JS, Molina A, Logothetis CJ, de Souza P, et al. Abiraterone in  
742 Metastatic Prostate Cancer without Previous Chemotherapy. *New England Journal of Medicine*.  
743 *Massachusetts Medical Society*; 2013;368:138–48.
- 744 5. Labrecque MP, Coleman IM, Brown LG, True LD, Kollath L, Lakely B, et al. Molecular profiling  
745 stratifies diverse phenotypes of treatment-refractory metastatic castration-resistant prostate cancer.  
746 *Journal of Clinical Investigation*. *American Society for Clinical Investigation*; 2019;129:4492–  
747 505.
- 748 6. Vlachostergios PJ, Puca L, Beltran H. Emerging Variants of Castration-Resistant Prostate Cancer.  
749 *Curr Oncol Rep*. *Current Medicine Group LLC* 1; 2017.
- 750 7. Beltran H, Prandi D, Mosquera JM, Benelli M, Puca L, Cyrta J, et al. Divergent clonal evolution  
751 of castration-resistant neuroendocrine prostate cancer. *Nat Med*. *Nature Publishing Group*;  
752 2016;22:298–305.
- 753 8. Aggarwal R, Huang J, Alumkal JJ, Zhang L, Feng FY, Thomas G v, et al. Clinical and Genomic  
754 Characterization of Treatment-Emergent Small-Cell Neuroendocrine Prostate Cancer: A Multi-  
755 institutional Prospective Study. *J Clin Oncol* [Internet]. 2018;36:2492–503. Available from:  
756 <https://doi.org/10.1200/JCO.2017>.
- 757 9. Bluemn EG, Coleman IM, Lucas JM, Coleman RT, Hernandez-Lopez S, Tharakan R, et al.  
758 Androgen Receptor Pathway-Independent Prostate Cancer Is Sustained through FGF Signaling.  
759 *Cancer Cell*. *Cell Press*; 2017;32:474-489.e6.
- 760 10. Westbrook TC, Guan X, Rodansky E, Flores D, Liu CJ, Udager AM, et al. Transcriptional  
761 profiling of matched patient biopsies clarifies molecular determinants of enzalutamide-induced  
762 lineage plasticity. *Nat Commun* [Internet]. *Nature Research*; 2022;13:5345. Available from:  
763 <http://www.ncbi.nlm.nih.gov/pubmed/36109521>
- 764 11. Robinson D, Van Allen EM, Wu Y-M, Schultz N, Lonigro RJ, Mosquera J-M, et al. Integrative  
765 clinical genomics of advanced prostate cancer. *Cell* [Internet]. *Cell Press*; 2015;161:1215–28.  
766 Available from: <http://www.ncbi.nlm.nih.gov/pubmed/26000489>
- 767 12. Quigley DA, Dang HX, Zhao SG, Lloyd P, Aggarwal R, Alumkal JJ, et al. Genomic Hallmarks  
768 and Structural Variation in Metastatic Prostate Cancer. *Cell*. *Cell Press*; 2018;174:758-769.e9.

- 769 13. Viswanathan SR, Ha G, Hoff AM, Wala JA, Carrot-Zhang J, Whelan CW, et al. Structural  
770 Alterations Driving Castration-Resistant Prostate Cancer Revealed by Linked-Read Genome  
771 Sequencing. *Cell*. Cell Press; 2018;174:433-447.e19.
- 772 14. Park JW, Lee JK, Sheu KM, Wang L, Balanis NG, Nguyen K, et al. Reprogramming normal  
773 human epithelial tissues to a common, lethal neuroendocrine cancer lineage [Internet]. Available  
774 from: <http://science.sciencemag.org/>
- 775 15. Pomerantz MM, Qiu X, Zhu Y, Takeda DY, Pan W, Baca SC, et al. Prostate cancer reactivates  
776 developmental epigenomic programs during metastatic progression. *Nat Genet*. Nature Research;  
777 2020;52:790–9.
- 778 16. Zhao SG, Chen WS, Li H, Foye A, Zhang M, Sjöström M, et al. The DNA methylation landscape  
779 of advanced prostate cancer. *Nat Genet*. Nature Research; 2020;52:778–89.
- 780 17. Sjöström M, Zhao SG, Levy S, Zhang M, Ning Y, Shrestha R, et al. The 5-  
781 Hydroxymethylcytosine Landscape of Prostate Cancer. *Cancer Res* [Internet]. 2022;82:3888–902.  
782 Available from: <http://www.ncbi.nlm.nih.gov/pubmed/36251389>
- 783 18. Rubin MA, Bristow RG, Thienger PD, Dive C, Imielinski M. Impact of Lineage Plasticity to and  
784 from a Neuroendocrine Phenotype on Progression and Response in Prostate and Lung Cancers.  
785 *Mol Cell* [Internet]. Cell Press; 2020;80:562–77. Available from:  
786 <http://www.ncbi.nlm.nih.gov/pubmed/33217316>
- 787 19. Stelloo S, Nevedomskaya E, Poel HG, Jong J, Leenders GJ, Jenster G, et al. Androgen receptor  
788 profiling predicts prostate cancer outcome. *EMBO Mol Med*. EMBO; 2015;7:1450–64.
- 789 20. Buenrostro JD, Giresi PG, Zaba LC, Chang HY, Greenleaf WJ. Transposition of native chromatin  
790 for fast and sensitive epigenomic profiling of open chromatin, DNA-binding proteins and  
791 nucleosome position. *Nat Methods*. 2013;10:1213–8.
- 792 21. Corces MR, Granja JM, Shams S, Louie BH, Seoane JA, Zhou W, et al. The chromatin  
793 accessibility landscape of primary human cancers. *Science* [Internet]. American Association for  
794 the Advancement of Science; 2018;362. Available from:  
795 <http://www.ncbi.nlm.nih.gov/pubmed/30361341>
- 796 22. Tang F, Xu D, Wang S, Wong CK, Martinez-Fundichely A, Lee CJ, et al. Chromatin profiles  
797 classify castration-resistant prostate cancers suggesting therapeutic targets. *Science* [Internet].  
798 American Association for the Advancement of Science; 2022;376:eabe1505. Available from:  
799 <http://www.ncbi.nlm.nih.gov/pubmed/35617398>
- 800 23. Corces MR, Trevino AE, Hamilton EG, Greenside PG, Sinnott-Armstrong NA, Vesuna S, et al.  
801 An improved ATAC-seq protocol reduces background and enables interrogation of frozen tissues.  
802 *Nat Methods*. Nature Publishing Group; 2017;14:959–62.
- 803 24. Martin M. Cutadapt removes adapter sequences from high-throughput sequencing reads. *EMBnet*  
804 *J* [Internet]. 2011;17:10–2. Available from:  
805 <https://journal.embnet.org/index.php/embnetjournal/article/view/200>
- 806 25. Andrews S. FastQC: A Quality Control Tool for High Throughput Sequence Data [Internet]. 2010.  
807 Available from: <http://www.bioinformatics.babraham.ac.uk/projects/fastqc/>

- 808 26. Langmead B, Salzberg SL. Fast gapped-read alignment with Bowtie 2. *Nat Methods*. 2012;9:357–  
809 9.
- 810 27. Li H, Handsaker B, Wysoker A, Fennell T, Ruan J, Homer N, et al. The Sequence Alignment/Map  
811 format and SAMtools. *Bioinformatics* [Internet]. Oxford Academic; 2009 [cited 2022 Nov  
812 9];25:2078–9. Available from:  
813 <https://academic.oup.com/bioinformatics/article/25/16/2078/204688>
- 814 28. Ramírez F, Ryan DP, Grüning B, Bhardwaj V, Kilpert F, Richter AS, et al. deepTools2: a next  
815 generation web server for deep-sequencing data analysis. *Nucleic Acids Res*. Oxford University  
816 Press; 2016;44:W160–5.
- 817 29. Zhang Y, Liu T, Meyer CA, Eeckhoute J, Johnson DS, Bernstein BE, et al. Model-based analysis  
818 of ChIP-Seq (MACS). *Genome Biol* [Internet]. 2008;9:R137. Available from:  
819 <http://www.ncbi.nlm.nih.gov/pubmed/18798982>
- 820 30. Yu G, Wang LG, He QY. ChIPseeker: an R/Bioconductor package for ChIP peak annotation,  
821 comparison and visualization. *Bioinformatics* [Internet]. Oxford Academic; 2015 [cited 2023 Mar  
822 18];31:2382–3. Available from:  
823 <https://academic.oup.com/bioinformatics/article/31/14/2382/255379>
- 824 31. Ou J, Liu H, Yu J, Kelliher MA, Castilla LH, Lawson ND, et al. ATACseqQC: a Bioconductor  
825 package for post-alignment quality assessment of ATAC-seq data. *BMC Genomics*. 2018;19:169.
- 826 32. Liao Y, Smyth GK, Shi W. The R package Rsubread is easier, faster, cheaper and better for  
827 alignment and quantification of RNA sequencing reads. *Nucleic Acids Res* [Internet]. Oxford  
828 Academic; 2019 [cited 2022 Nov 9];47:e47–e47. Available from:  
829 <https://academic.oup.com/nar/article/47/8/e47/5345150>
- 830 33. Love MI, Huber W, Anders S. Moderated estimation of fold change and dispersion for RNA-seq  
831 data with DESeq2. *Genome Biol* [Internet]. BioMed Central Ltd.; 2014 [cited 2022 Nov 9];15:1–  
832 21. Available from: [https://genomebiology.biomedcentral.com/articles/10.1186/s13059-014-0550-](https://genomebiology.biomedcentral.com/articles/10.1186/s13059-014-0550-8)  
833 8
- 834 34. McLean CY, Bristor D, Hiller M, Clarke SL, Schaar BT, Lowe CB, et al. GREAT improves  
835 functional interpretation of cis-regulatory regions. *Nat Biotechnol* [Internet]. 2010;28:495–501.  
836 Available from: <http://www.ncbi.nlm.nih.gov/pubmed/20436461>
- 837 35. Liberzon A, Birger C, Thorvaldsdóttir H, Ghandi M, Mesirov JP, Tamayo P. The Molecular  
838 Signatures Database Hallmark Gene Set Collection. *Cell Syst*. Cell Press; 2015;1:417–25.
- 839 36. Bhuva DD, Cursons J, Davis MJ. Stable gene expression for normalisation and single-sample  
840 scoring. *Nucleic Acids Res*. 2020;48:e113.
- 841 37. Bentsen M, Goymann P, Schultheis H, Klee K, Petrova A, Wiegandt R, et al. ATAC-seq  
842 footprinting unravels kinetics of transcription factor binding during zygotic genome activation.  
843 *Nat Commun* [Internet]. Nature Research; 2020;11:4267. Available from:  
844 <http://www.ncbi.nlm.nih.gov/pubmed/32848148>
- 845 38. Castro-Mondragon JA, Riudavets-Puig R, Rauluseviciute I, Lemma RB, Turchi L, Blanc-Mathieu  
846 R, et al. JASPAR 2022: the 9th release of the open-access database of transcription factor binding  
847 profiles. *Nucleic Acids Res*. 2022;50:D165–73.

- 848 39. Wilson S, Qi J, Filipp F V. Refinement of the androgen response element based on ChIP-Seq in  
849 androgen-insensitive and androgen-responsive prostate cancer cell lines. *Sci Rep* [Internet]. Nature  
850 Publishing Group; 2016;6:32611. Available from: <https://www.nature.com/articles/srep32611>
- 851 40. Pinskaya M, Saci Z, Gallopin M, Gabriel M, Nguyen HT, Firlej V, et al. Reference-free  
852 transcriptome exploration reveals novel RNAs for prostate cancer diagnosis. *Life Sci Alliance*.  
853 2019;2.
- 854 41. Chen S, Huang V, Xu X, Livingstone J, Soares F, Jeon J, et al. Widespread and Functional RNA  
855 Circularization in Localized Prostate Cancer. *Cell*. 2019;176:831-843.e22.
- 856 42. Cejas P, Xie Y, Font-Tello A, Lim K, Syamala S, Qiu X, et al. Subtype heterogeneity and  
857 epigenetic convergence in neuroendocrine prostate cancer. *Nat Commun. Nature Research*;  
858 2021;12.
- 859 43. Imbeault M, Helleboid PY, Trono D. KRAB zinc-finger proteins contribute to the evolution of  
860 gene regulatory networks. *Nature*. Nature Publishing Group; 2017;543:550–4.
- 861 44. Frieze S, Lan X, Jin VX, Farnham PJ. Genomic targets of the KRAB and SCAN domain-  
862 containing zinc finger protein 263. *J Biol Chem* [Internet]. 2010;285:1393–403. Available from:  
863 <http://www.ncbi.nlm.nih.gov/pubmed/19887448>
- 864 45. Pope BD, Ryba T, Dileep V, Yue F, Wu W, Denas O, et al. Topologically associating domains are  
865 stable units of replication-timing regulation. *Nature* [Internet]. *Nature*; 2014 [cited 2023 Mar  
866 27];515:402–5. Available from: <https://pubmed.ncbi.nlm.nih.gov/25409831/>
- 867 46. Barfeld SJ, Urbanucci A, Itkonen HM, Fazli L, Hicks JL, Thiede B, et al. c-Myc Antagonises the  
868 Transcriptional Activity of the Androgen Receptor in Prostate Cancer Affecting Key Gene  
869 Networks. *EBioMedicine* [Internet]. *EBioMedicine*; 2017 [cited 2023 Mar 27];18:83–93.  
870 Available from: <https://pubmed.ncbi.nlm.nih.gov/28412251/>
- 871 47. See YX, Chen K, Fullwood MJ. MYC overexpression leads to increased chromatin interactions at  
872 super-enhancers and MYC binding sites. *Genome Res* [Internet]. *Genome Res*; 2022 [cited 2023  
873 Mar 27];32:629–42. Available from: <https://pubmed.ncbi.nlm.nih.gov/35115371/>
- 874 48. Guo H, Wu Y, Nouri M, Spisak S, Russo JW, Sowalsky AG, et al. Androgen receptor and MYC  
875 equilibration centralizes on developmental super-enhancer. *Nat Commun* [Internet]. *Nat Commun*;  
876 2021 [cited 2023 Mar 27];12. Available from: <https://pubmed.ncbi.nlm.nih.gov/34911936/>
- 877 49. Oki S, Ohta T, Shioi G, Hatanaka H, Ogasawara O, Okuda Y, et al. ChIP-Atlas: a data-mining  
878 suite powered by full integration of public ChIP-seq data. *EMBO Rep*. 2018;19.
- 879 50. Urbanucci A, Barfeld SJ, Kytölä V, Itkonen HM, Coleman IM, Vodák D, et al. Androgen  
880 Receptor Deregulation Drives Bromodomain-Mediated Chromatin Alterations in Prostate Cancer.  
881 *Cell Rep*. Elsevier B.V.; 2017;19:2045–59.
- 882 51. Lundberg A, Zhang M, Aggarwal R, Li H, Zhang L, Foye A, et al. The genomic and epigenomic  
883 landscape of double-negative metastatic prostate cancer. *Cancer Res*. 2023;
- 884 52. Meyer RC, Giddens MM, Schaefer SA, Hall RA. GPR37 and GPR37L1 are receptors for the  
885 neuroprotective and glioprotective factors prosaptide and prosaposin. *Proc Natl Acad Sci U S A*



- 886 [Internet]. Proc Natl Acad Sci U S A; 2013 [cited 2023 Apr 6];110:9529–34. Available from:  
887 <https://pubmed.ncbi.nlm.nih.gov/23690594/>
- 888 53. Vierstra J, Stamatoyannopoulos JA. Genomic footprinting. Nat Methods [Internet]. Nature  
889 Publishing Group; 2016;13:213–21. Available from:  
890 <http://www.ncbi.nlm.nih.gov/pubmed/26914205>
- 891 54. Castro-Mondragon JA, Riudavets-Puig R, Rauluseviciute I, Berhanu Lemma R, Turchi L, Blanc-  
892 Mathieu R, et al. JASPAR 2022: the 9th release of the open-access database of transcription factor  
893 binding profiles. Nucleic Acids Res [Internet]. Nucleic Acids Res; 2022 [cited 2022 Nov  
894 29];50:D165–73. Available from: <https://pubmed.ncbi.nlm.nih.gov/34850907/>
- 895 55. Nouruzi S, Ganguli D, Tabrizian N, Kobelev M, Sivak O, Namekawa T, et al. ASCL1 activates  
896 neuronal stem cell-like lineage programming through remodeling of the chromatin landscape in  
897 prostate cancer. Nat Commun. Nature Research; 2022;13.
- 898 56. Bishop JL, Thaper D, Vahid S, Davies A, Ketola K, Kuruma H, et al. The master neural  
899 transcription factor BRN2 is an androgen receptor–suppressed driver of neuroendocrine  
900 differentiation in prostate cancer. Cancer Discov. American Association for Cancer Research Inc.;  
901 2017;7:54–71.
- 902 57. FitsGerald PC, Shlyakhtenko A, Mir AA, Vinson C. Clustering of DNA sequences in human  
903 promoters. Genome Res [Internet]. Genome Res; 2004 [cited 2023 Mar 21];14:1562–74. Available  
904 from: <https://pubmed.ncbi.nlm.nih.gov/15256515/>
- 905 58. Sahu B, Laakso M, Ovaska K, Mirtti T, Lundin J, Rannikko A, et al. Dual role of FoxA1 in  
906 androgen receptor binding to chromatin, androgen signalling and prostate cancer. EMBO J.  
907 2011;30:3962–76.
- 908 59. Grasso CS, Wu YM, Robinson DR, Cao X, Dhanasekaran SM, Khan AP, et al. The mutational  
909 landscape of lethal castration-resistant prostate cancer. Nature. 2012;487:239–43.
- 910 60. Bery F, Cancel M, Guéguinou M, Potier-Cartereau M, Vandier C, Chantôme A, et al. Zeb1 and  
911 SK3 Channel Are Up-Regulated in Castration-Resistant Prostate Cancer and Promote  
912 Neuroendocrine Differentiation. Cancers (Basel) [Internet]. Cancers (Basel); 2021 [cited 2023 Mar  
913 22];13. Available from: <https://pubmed.ncbi.nlm.nih.gov/34204608/>
- 914 61. Lee GT, Rosenfeld JA, Kim WT, Kwon YS, Palapattu G, Mehra R, et al. TCF4 induces  
915 enzalutamide resistance via neuroendocrine differentiation in prostate cancer. PLoS One  
916 [Internet]. PLoS One; 2019 [cited 2023 Mar 22];14. Available from:  
917 <https://pubmed.ncbi.nlm.nih.gov/31536510/>
- 918 62. Cmero M, Kurganovs NJ, Stuchbery R, McCoy P, Grima C, Ngyuen A, et al. Loss of SNAI2 in  
919 Prostate Cancer Correlates With Clinical Response to Androgen Deprivation Therapy. JCO Precis  
920 Oncol [Internet]. JCO Precis Oncol; 2021 [cited 2023 Mar 22];5:1048–59. Available from:  
921 <https://pubmed.ncbi.nlm.nih.gov/34322653/>
- 922 63. Zhao Y, Vartak S v., Conte A, Wang X, Garcia DA, Stevens E, et al. “Stripe” transcription factors  
923 provide accessibility to co-binding partners in mammalian genomes. Mol Cell. Cell Press;  
924 2022;82:3398-3411.e11.

- 925 64. Che M, Chaturvedi A, Munro SA, Pitzen SP, Ling A, Zhang W, et al. Opposing transcriptional  
926 programs of KLF5 and AR emerge during therapy for advanced prostate cancer. *Nat Commun*  
927 [Internet]. *Nature Research*; 2021;12:6377. Available from:  
928 <http://www.ncbi.nlm.nih.gov/pubmed/34737261>
- 929 65. Cui J, Liu J, Fan L, Zhu Y, Zhou B, Wang Y, et al. A zinc finger family protein, ZNF263,  
930 promotes hepatocellular carcinoma resistance to apoptosis via activation of ER stress-dependent  
931 autophagy. *Transl Oncol* [Internet]. *Neoplasia Press, Inc.*; 2020;13:100851. Available from:  
932 <http://www.ncbi.nlm.nih.gov/pubmed/32898766>
- 933 66. Yu Z, Feng J, Wang W, Deng Z, Zhang Y, Xiao L, et al. The EGFR-ZNF263 signaling axis  
934 silences SIX3 in glioblastoma epigenetically. *Oncogene* [Internet]. *Springer Nature*;  
935 2020;39:3163–78. Available from: <http://www.ncbi.nlm.nih.gov/pubmed/32051553>
- 936 67. Thurman RE, Rynes E, Humbert R, Vierstra J, Maurano MT, Haugen E, et al. The accessible  
937 chromatin landscape of the human genome. *Nature* [Internet]. 2012;489:75–82. Available from:  
938 <http://www.ncbi.nlm.nih.gov/pubmed/22955617>
- 939 68. Samarasinghe KTG, Jaime-Figueroa S, Burgess M, Nalawansa DA, Dai K, Hu Z, et al. Targeted  
940 degradation of transcription factors by TRAFACs: TRAnscription Factor TArgeting Chimeras.  
941 *Cell Chem Biol*. Elsevier Ltd; 2021;28:648-661.e5.
- 942 69. Henley MJ, Koehler AN. Advances in targeting ‘undruggable’ transcription factors with small  
943 molecules. *Nat Rev Drug Discov*. *Nature Research*; 2021. page 669–88.
- 944
- 945

## 946 **Figure Legends**

947 **Figure 1. Chromatin accessibility changes during prostate cancer progression affect stage-specific**  
948 **regulatory elements.** (a) Principal component analysis (PCA) of the ATAC-seq profiles comparing different  
949 stages of prostate cancer including benign prostate, localized prostate cancer (PCa), mCRPC Adeno, and  
950 mCRPC t-SCNC. The normalized read counts of these consensus-accessible regions were used for the PCA  
951 analysis. Each dot in the plot represents an individual sample. (b) An alluvial plot demonstrating changes  
952 in accessible chromatin regions in various stages of prostate cancer. Each bar corresponds to a distinct PCA  
953 stage, with the orange and white sections indicating accessible and inaccessible chromatin regions,  
954 respectively. The shaded areas connecting the bars represent changes in the accessibility of these  
955 chromatin regions. The pink and blue shaded regions respectively represent accessible and inaccessible  
956 chromatin regions in mCRPC Adeno. (c) Heatmap representation of the chromatin between different  
957 stages. The rows are segregated by the chromatin variants in each stage. (d) The percentage of chromatin  
958 variants in mCRPC Adeno. The ATAC-seq peaks are grouped by the genomic regions (promoter, intron,  
959 or distal intergenic) to which they are mapped. (e) ATAC-seq profile plot illustrating potential regulatory  
960 regions in chromatin variants in mCRPC Adeno. The profile plot represents the overlapping region  
961 between the chromatin variants and publicly available H3K27ac ChIP-seq data from mCRPC PDX. (f)  
962 Enrichment of chromatin regions exclusively accessible in localized PCa, mCRPC Adeno, or mCRPC t-  
963 SCNC against GO Biological Processes.

964 **Figure 2. Chromatin accessibility in mCRPC is associated with subtypes linked to androgen**  
965 **signaling.** (a) Unsupervised hierarchical clustering of pairwise sample Spearman's correlation based on  
966 the normalized read counts of consensus ATAC-seq peaks of mCRPC. (b-c) Distribution of (b) androgen  
967 receptor (AR) pathway score, (c) neuroendocrine (NE) score calculated based on RNA-seq gene expression  
968 profiles of mCRPCs classified into individual clusters in Figure 2a. Statistically significant Wilcoxon rank  
969 sum test p-values between the clusters are indicated in the plot.

970 **Figure 3. mCRPC transcriptional subtypes are associated with chromatin variants of prostate**  
971 **cancer signaling pathways.** (a) Heatmap of chromatin variants between mCRPC transcriptional subtypes.  
972 (b) ATAC-seq peaks around *AR*, *NKX3-1*, and *GPR37LI* gene regions. The highlighted vertical strip  
973 illustrates the presence of ATAC-seq peaks at the enhancer region. (c) Heatmap representation of the  
974 chromatin variants between mCRPC transcriptional subtypes. The rows are segregated by the differential  
975 regions mapped to gene promoter, intron, or distal intergenic regions. (d-f) Hallmark pathways enrichment  
976 of chromatin variants between the mCRPC transcriptional subtypes mapped to (d) promoter, (e) intron, and  
977 (f) distal intergenic regions identified using GREAT enrichment analysis (see Methods section).

978 **Figure 4. mCRPC transcriptional subtypes are defined by DNA accessibility-guided patterns of**  
979 **transcription factor regulation.** (a-b) ATAC-seq TF (*AR* and *HOXB13*) footprints signal difference  
980 between TF-bound and unbound sites. (c-d) Volcano plot of differential TF footprint occupancy analysis  
981 comparing the (c) AR+NE- and AR-NE+ subtypes and (d) AR+NE- and AR-NE- subtypes. Each dot in the  
982 plot represents a TF motif. The colored dots indicate a significantly differentially bound TF motif. (Data  
983 available as Supplementary Table S4) (e) Heatmap of genome-wide active TF occupancy, determined by TF  
984 footprints, associated with different mCRPC transcriptional subtypes. Each rim of the circular heatmap  
985 represents an individual mCRPC transcriptional subtype and the sector represents TF. The darker color  
986 shade indicates the strong association of the TF with the respective mCRPC subtype. See the Methods

987 section for details on TF occupancy phenotype score calculation.

988 **Figure 5. Identification of the influential transcription factors driving mCRPC transcriptional**  
989 **subtypes.** We hypothesized that highly active TF regulate (or influence) gene expression activity of a large  
990 fraction of target genes. The plot indicates the top influential mCRPC transcriptional subtype-associated TFs  
991 ranked by the number of target genes (based on gene expression) they influence.

992 **Figure 6. ZNF263 activates MYC signaling targets.** (a) The volcano plot depicts the genes that undergo  
993 activation or repression upon *ZNF263* binding to their specific promoter region. Each gene is represented  
994 by a dot, and the difference in gene expression between samples with and without *ZNF263* in the promoter  
995 region was measured as fold change. Additionally, the statistical significance of the difference was  
996 evaluated using the Wilcoxon rank sum test to calculate the p-value between the two groups. (b) Over-  
997 representation analysis of the predicted *ZNF263* target genes against the Hallmark pathways. (c) Percentage  
998 of the predicted target genes of *MYC* that overlap with those of TFs associated with AR-NE- subtype. The  
999 overlap of the respective TF target genes with genes in the Hallmark *MYC* targets geneset is illustrated as  
1000 the red line. (d) Heatmap of overlapping *ZNF263* and *MYC* footprint sites. The red color highlights the  
1001 direct overlap between *ZNF263* and *MYC* footprints. (e) Volcano plot showing the genes that are activated  
1002 when *ZNF263* binds to the promoter region compared to genes that are activated with both *ZNF263* and *MYC*  
1003 are not bound to the promoter region. (f) Box plot of gene expression foldchange when different  
1004 combinations of *ZNF263* and *MYC* bind to the promoter as compared to when both *ZNF263* and *MYC* are  
1005 simultaneously absent in the promoter. Each dot represents a gene in Hallmark *MYC* targets geneset.

Figure 1

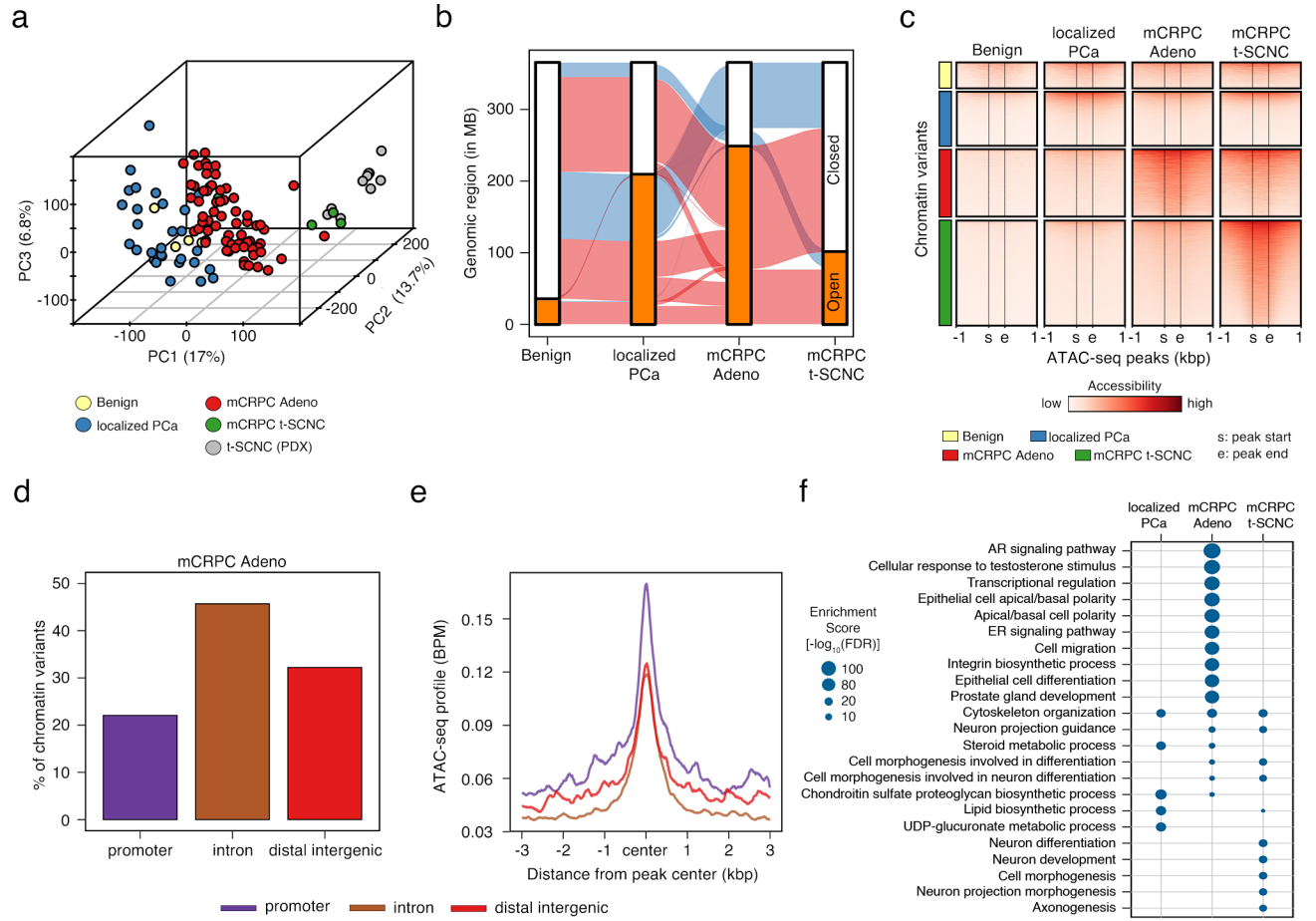


Figure 2

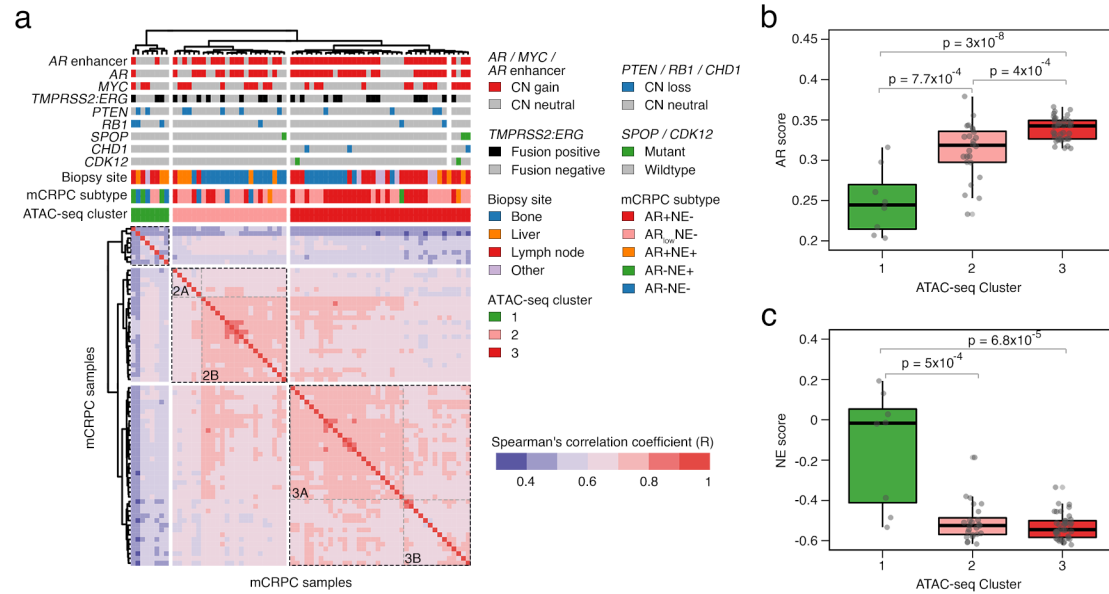


Figure 3

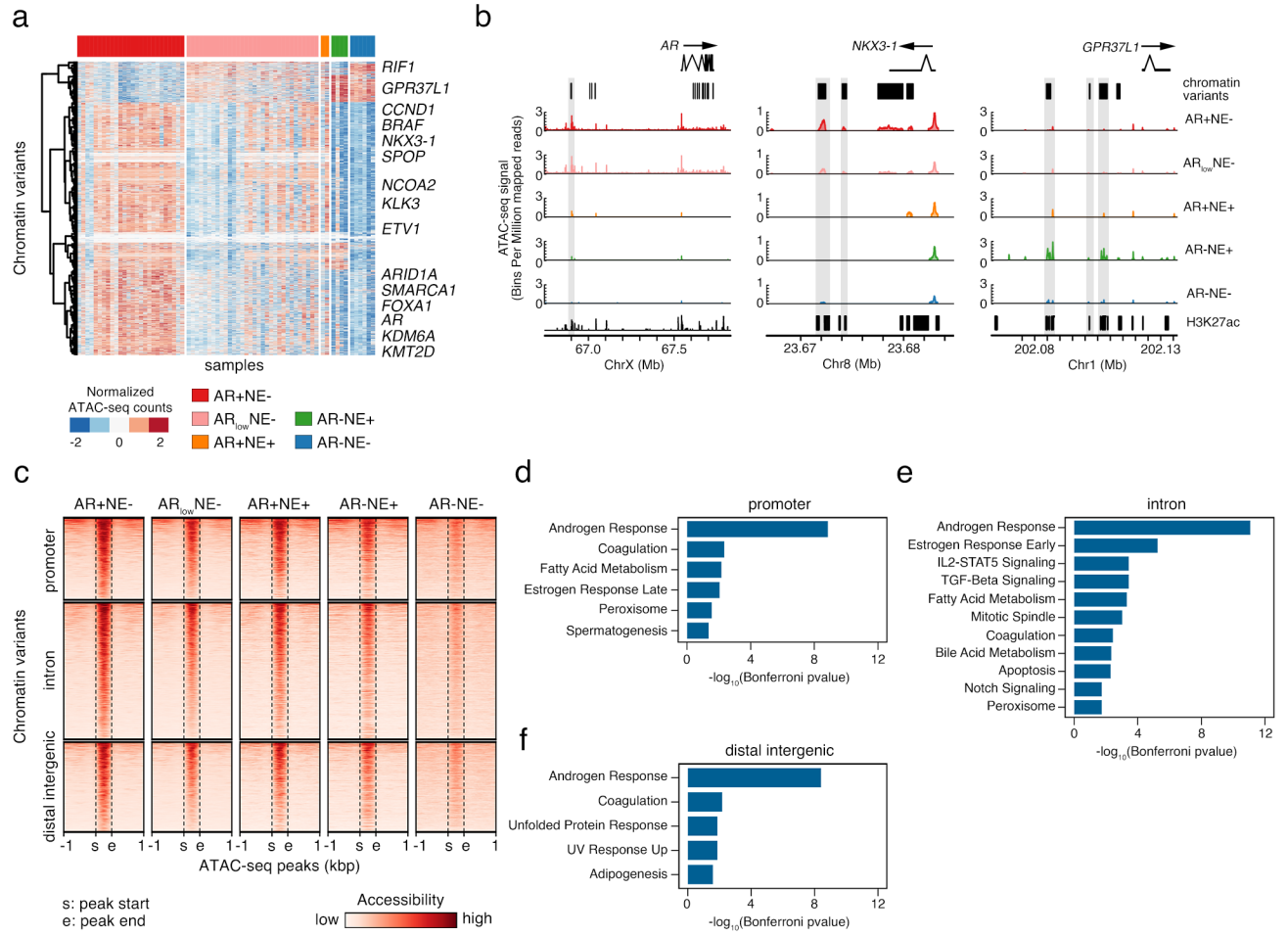


Figure 4

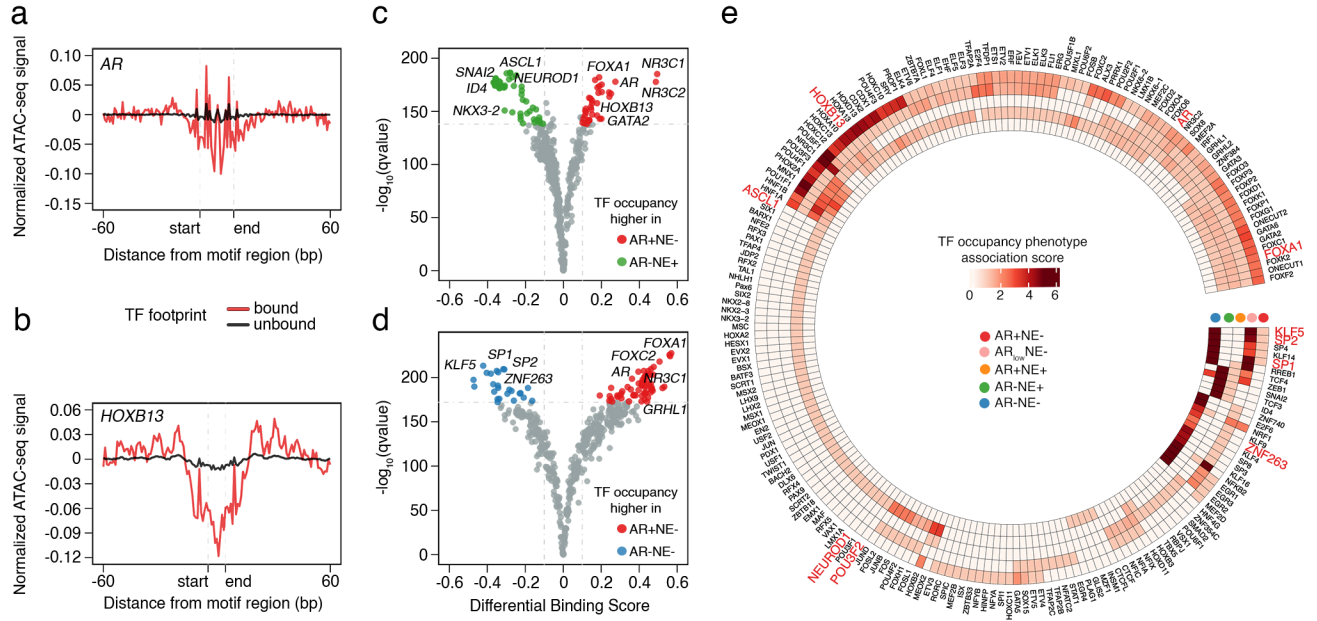




Figure 5

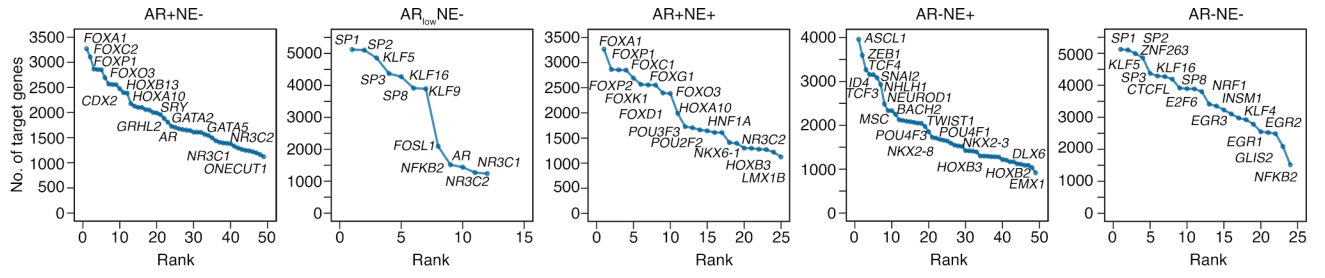
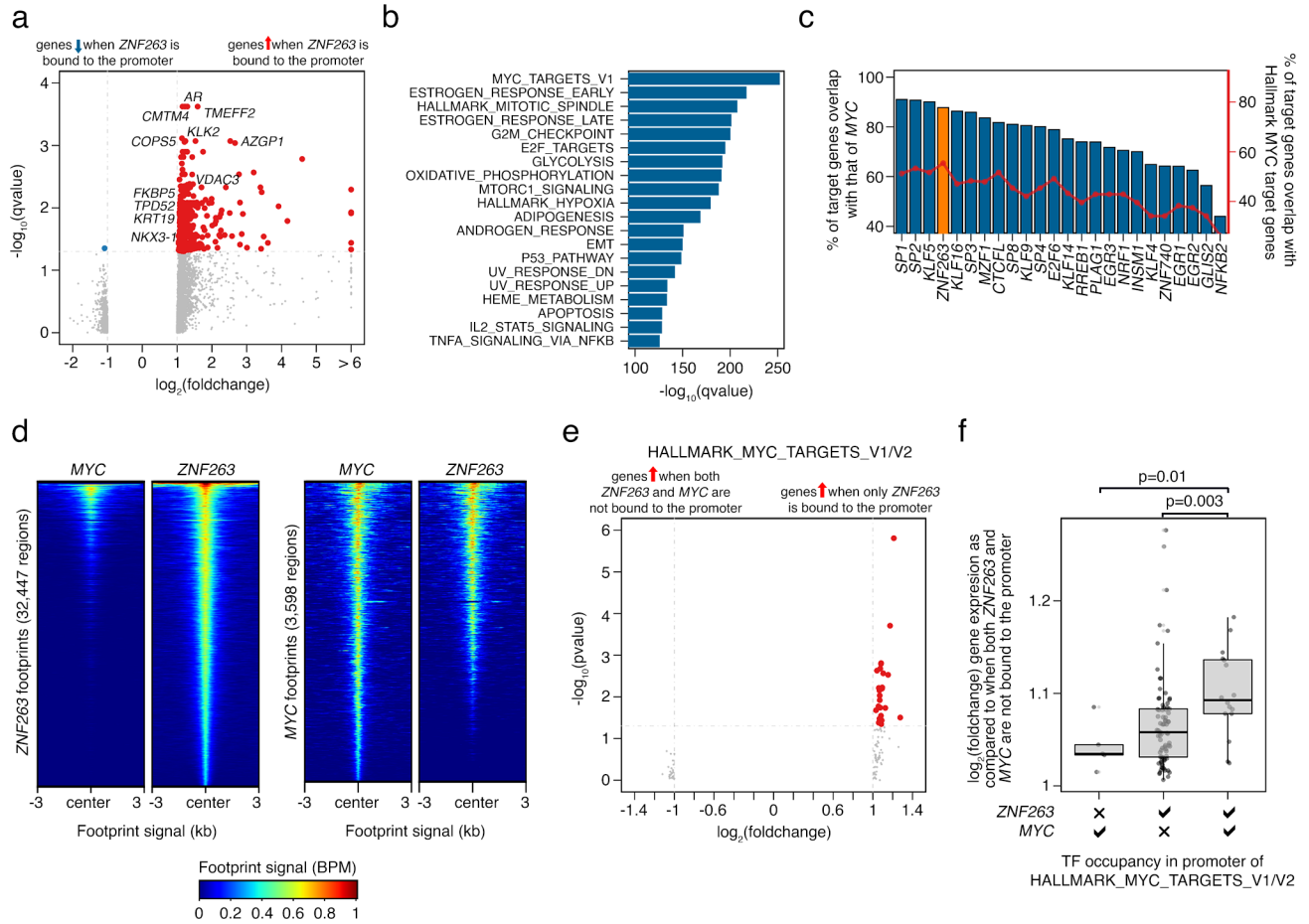


Figure 6



## Parsed Citations

1. Siegel RL, Miller KD, Fuchs HE, Jemal A. Cancer statistics, 2022. *CA Cancer J Clin* [Internet]. American Cancer Society; 2022 [cited 2022 Dec 23];72:7-33. Available from: <https://onlinelibrary.wiley.com/doi/full/10.3322/caac.21708>

Pubmed: [Author and Title](#)

Google Scholar: [Google Scholar Search](#)

2. de Bono JS, Logothetis CJ, Molina A, Fizazi K, North S, Chu L, et al. Abiraterone and Increased Survival in Metastatic Prostate Cancer. *n engl j med*. 2011.

Pubmed: [Author and Title](#)

Google Scholar: [Google Scholar Search](#)

3. Scher HI, Fizazi K, Saad F, Taplin M-E, Sternberg CN, Miller K, et al. Increased Survival with Enzalutamide in Prostate Cancer after Chemotherapy. *New England Journal of Medicine*. New England Journal of Medicine (NEJM/MMS); 2012;367:1187-97.

Pubmed: [Author and Title](#)

Google Scholar: [Google Scholar Search](#)

4. Ryan CJ, Smith MR, de Bono JS, Molina A, Logothetis CJ, de Souza P, et al. Abiraterone in Metastatic Prostate Cancer without Previous Chemotherapy. *New England Journal of Medicine*. Massachusetts Medical Society; 2013;368:138-48.

Pubmed: [Author and Title](#)

Google Scholar: [Google Scholar Search](#)

5. Labrecque MP, Coleman IM, Brown LG, True LD, Kollath L, Lakely B, et al. Molecular profiling stratifies diverse phenotypes of treatment-refractory metastatic castration-resistant prostate cancer. *Journal of Clinical Investigation*. American Society for Clinical Investigation; 2019;129:4492- 505.

Pubmed: [Author and Title](#)

Google Scholar: [Google Scholar Search](#)

6. Vlachostergios PJ, Puca L, Beltran H. Emerging Variants of Castration-Resistant Prostate Cancer. *Curr Oncol Rep*. Current Medicine Group LLC 1; 2017.

Pubmed: [Author and Title](#)

Google Scholar: [Google Scholar Search](#)

7. Beltran H, Prandi D, Mosquera JM, Benelli M, Puca L, Cyrta J, et al. Divergent clonal evolution of castration-resistant neuroendocrine prostate cancer. *Nat Med*. Nature Publishing Group; 2016;22:298-305.

Pubmed: [Author and Title](#)

Google Scholar: [Google Scholar Search](#)

8. Aggarwal R, Huang J, Alumkal JJ, Zhang L, Feng FY, Thomas G v, et al. Clinical and Genomic Characterization of Treatment-Emergent Small-Cell Neuroendocrine Prostate Cancer: A Multi-institutional Prospective Study. *J Clin Oncol* [Internet]. 2018;36:2492-503. Available from: <https://doi.org/10.1200/JCO.2017>.

Pubmed: [Author and Title](#)

Google Scholar: [Google Scholar Search](#)

9. Bluemn EG, Coleman IM, Lucas JM, Coleman RT, Hernandez-Lopez S, Tharakan R, et al. Androgen Receptor Pathway-Independent Prostate Cancer Is Sustained through FGF Signaling. *Cancer Cell*. Cell Press; 2017;32:474-489.e6.

Pubmed: [Author and Title](#)

Google Scholar: [Google Scholar Search](#)

10. Westbrook TC, Guan X, Rodansky E, Flores D, Liu CJ, Udager AM, et al. Transcriptional profiling of matched patient biopsies clarifies molecular determinants of enzalutamide-induced lineage plasticity. *Nat Commun* [Internet]. Nature Research; 2022;13:5345. Available from: <http://www.ncbi.nlm.nih.gov/pubmed/36109521>

Pubmed: [Author and Title](#)

Google Scholar: [Google Scholar Search](#)

**11. Robinson D, Van Allen EM, Wu Y-M, Schultz N, Lonigro RJ, Mosquera J-M, et al. Integrative clinical genomics of advanced prostate cancer. Cell [Internet]. Cell Press; 2015;161:1215-28. Available from: <http://www.ncbi.nlm.nih.gov/pubmed/26000489>**

Pubmed: [Author and Title](#)

Google Scholar: [Google Scholar Search](#)

**12. Quigley DA, Dang HX, Zhao SG, Lloyd P, Aggarwal R, Alumkal JJ, et al. Genomic Hallmarks and Structural Variation in Metastatic Prostate Cancer. Cell. Cell Press; 2018;174:758-769.e9.**

Pubmed: [Author and Title](#)

Google Scholar: [Google Scholar Search](#)

**13. Viswanathan SR, Ha G, Hoff AM, Wala JA, Carrot-Zhang J, Whelan CW, et al. Structural Alterations Driving Castration-Resistant Prostate Cancer Revealed by Linked-Read Genome Sequencing. Cell. Cell Press; 2018;174:433-447.e19.**

Pubmed: [Author and Title](#)

Google Scholar: [Google Scholar Search](#)

**14. Park JW, Lee JK, Sheu KM, Wang L, Balanis NG, Nguyen K, et al. Reprogramming normal human epithelial tissues to a common, lethal neuroendocrine cancer lineage [Internet]. Available from: <http://science.sciencemag.org/>**

**15. Pomerantz MM, Qiu X, Zhu Y, Takeda DY, Pan W, Baca SC, et al. Prostate cancer reactivates developmental epigenomic programs during metastatic progression. Nat Genet. Nature Research; 2020;52:790-9.**

Pubmed: [Author and Title](#)

Google Scholar: [Google Scholar Search](#)

**16. Zhao SG, Chen WS, Li H, Foye A, Zhang M, Sjöström M, et al. The DNA methylation landscape of advanced prostate cancer. Nat Genet. Nature Research; 2020;52:778-89.**

Pubmed: [Author and Title](#)

Google Scholar: [Google Scholar Search](#)

**17. Sjöström M, Zhao SG, Levy S, Zhang M, Ning Y, Shrestha R, et al. The 5-Hydroxymethylcytosine Landscape of Prostate Cancer. Cancer Res [Internet]. 2022;82:3888-902. Available from: <http://www.ncbi.nlm.nih.gov/pubmed/36251389>**

Pubmed: [Author and Title](#)

Google Scholar: [Google Scholar Search](#)

**18. Rubin MA, Bristow RG, Thienger PD, Dive C, Imielinski M. Impact of Lineage Plasticity to and from a Neuroendocrine Phenotype on Progression and Response in Prostate and Lung Cancers. Mol Cell [Internet]. Cell Press; 2020;80:562-77. Available from: <http://www.ncbi.nlm.nih.gov/pubmed/33217316>**

Pubmed: [Author and Title](#)

Google Scholar: [Google Scholar Search](#)

**19. Stelloo S, Nevedomskaya E, Poel HG, Jong J, Leenders GJ, Jenster G, et al. Androgen receptor profiling predicts prostate cancer outcome. EMBO Mol Med. EMBO; 2015;7:1450-64.**

Pubmed: [Author and Title](#)

Google Scholar: [Google Scholar Search](#)

**20. Buenrostro JD, Giresi PG, Zaba LC, Chang HY, Greenleaf WJ. Transposition of native chromatin for fast and sensitive epigenomic profiling of open chromatin, DNA-binding proteins and nucleosome position. Nat Methods. 2013;10:1213-8.**

Pubmed: [Author and Title](#)

Google Scholar: [Google Scholar Search](#)

**21. Corces MR, Granja JM, Shams S, Louie BH, Seoane JA, Zhou W, et al. The chromatin accessibility landscape of primary human cancers. Science [Internet]. American Association for the Advancement of Science; 2018;362. Available from: <http://www.ncbi.nlm.nih.gov/pubmed/30361341>**

Pubmed: [Author and Title](#)

Google Scholar: [Google Scholar Search](#)

**22. Tang F, Xu D, Wang S, Wong CK, Martinez-Fundichely A, Lee CJ, et al. Chromatin profiles classify castration-resistant prostate cancers suggesting therapeutic targets. Science [Internet]. American Association for the Advancement of Science; 2022;376:eabe1505. Available from: <http://www.ncbi.nlm.nih.gov/pubmed/35617398>**

Pubmed: [Author and Title](#)

Google Scholar: [Google Scholar Search](#)

**23. Corces MR, Trevino AE, Hamilton EG, Greenside PG, Sinnott-Armstrong NA, Vesuna S, et al. An improved ATAC-seq protocol reduces background and enables interrogation of frozen tissues. Nat Methods. Nature Publishing Group; 2017;14:959-62.**

Pubmed: [Author and Title](#)

Google Scholar: [Google Scholar Search](#)

**24. Martin M. Cutadapt removes adapter sequences from high-throughput sequencing reads. EMBnet J [Internet]. 2011;17:10-2. Available from: <https://journal.embnet.org/index.php/embnetjournal/article/view/200>**

Pubmed: [Author and Title](#)

Google Scholar: [Google Scholar Search](#)

**25. Andrews S. FastQC: A Quality Control Tool for High Throughput Sequence Data [Internet]. 2010. Available from: <http://www.bioinformatics.babraham.ac.uk/projects/fastqc/>**

**26. Langmead B, Salzberg SL. Fast gapped-read alignment with Bowtie 2. Nat Methods. 2012;9:357-**

Pubmed: [Author and Title](#)

Google Scholar: [Google Scholar Search](#)

**9.**

**27. Li H, Handsaker B, Wysoker A, Fennell T, Ruan J, Homer N, et al. The Sequence Alignment/Map format and SAMtools. Bioinformatics [Internet]. Oxford Academic; 2009 [cited 2022 Nov**

**9. ;25:2078-9. Available from: <https://academic.oup.com/bioinformatics/article/25/16/2078/204688>**

Pubmed: [Author and Title](#)

Google Scholar: [Google Scholar Search](#)

**28. Ramirez F, Ryan DP, Gruning B, Bhardwaj V, Kilpert F, Richter AS, et al. deepTools2: a next generation web server for deep-sequencing data analysis. Nucleic Acids Res. Oxford University Press; 2016;44:W160-5.**

Pubmed: [Author and Title](#)

Google Scholar: [Google Scholar Search](#)

**29. Zhang Y, Liu T, Meyer CA, Eeckhoute J, Johnson DS, Bernstein BE, et al. Model-based analysis of ChIP-Seq (MACS). Genome Biol [Internet]. 2008;9:R137. Available from: <http://www.ncbi.nlm.nih.gov/pubmed/18798982>**

Pubmed: [Author and Title](#)

Google Scholar: [Google Scholar Search](#)

**30. Yu G, Wang LG, He QY. ChIPseeker: an R/Bioconductor package for ChIP peak annotation, comparison and visualization. Bioinformatics [Internet]. Oxford Academic; 2015 [cited 2023 Mar**

**18. ;31:2382-3. Available from: <https://academic.oup.com/bioinformatics/article/31/14/2382/255379>**

Pubmed: [Author and Title](#)

Google Scholar: [Google Scholar Search](#)

**31. Ou J, Liu H, Yu J, Kelliher MA, Castilla LH, Lawson ND, et al. ATACseqQC: a Bioconductor package for post-alignment quality assessment of ATAC-seq data. BMC Genomics. 2018;19:169.**

Pubmed: [Author and Title](#)

Google Scholar: [Google Scholar Search](#)

**32. Liao Y, Smyth GK, Shi W. The R package Rsubread is easier, faster, cheaper and better for alignment and quantification of RNA sequencing reads. Nucleic Acids Res [Internet]. Oxford Academic; 2019 [cited 2022 Nov 9];47:e47-e47. Available from: <https://academic.oup.com/nar/article/47/8/e47/5345150>**

Pubmed: [Author and Title](#)

Google Scholar: [Google Scholar Search](#)

**33. Love MI, Huber W, Anders S. Moderated estimation of fold change and dispersion for RNA-seq data with DESeq2. Genome Biol [Internet]. BioMed Central Ltd.; 2014 [cited 2022 Nov 9];15:1-**

**21. Available from: <https://genomebiology.biomedcentral.com/articles/10.1186/s13059-014-0550->**

**34. McLean CY, Bristor D, Hiller M, Clarke SL, Schaar BT, Lowe CB, et al. GREAT improves functional interpretation of cis-regulatory regions. Nat Biotechnol [Internet]. 2010;28:495-501. Available from: <http://www.ncbi.nlm.nih.gov/pubmed/20436461>**

Pubmed: [Author and Title](#)

Google Scholar: [Google Scholar Search](#)

**35. Liberzon A, Birger C, Thorvaldsdottir H, Ghandi M, Mesirov JP, Tamayo P. The Molecular Signatures Database Hallmark Gene Set Collection. Cell Syst. Cell Press; 2015;1:417-25.**

Pubmed: [Author and Title](#)

Google Scholar: [Google Scholar Search](#)

**36. Bhuvu DD, Cursons J, Davis MJ. Stable gene expression for normalisation and single-sample scoring. Nucleic Acids Res. 2020;48:e113.**

Pubmed: [Author and Title](#)

Google Scholar: [Google Scholar Search](#)

**37. Bentsen M, Goymann P, Schultheis H, Klee K, Petrova A, Wiegandt R, et al. ATAC-seq footprinting unravels kinetics of transcription factor binding during zygotic genome activation. Nat Commun [Internet]. Nature Research; 2020;11:4267. Available from: <http://www.ncbi.nlm.nih.gov/pubmed/32848148>**

Pubmed: [Author and Title](#)

Google Scholar: [Google Scholar Search](#)

**38. Castro-Mondragon JA, Riudavets-Puig R, Rauluseviciute I, Lemma RB, Turchi L, Blanc-Mathieu R, et al. JASPAR 2022: the 9th release of the open-access database of transcription factor binding profiles. Nucleic Acids Res. 2022;50:D165-73.**

Pubmed: [Author and Title](#)

Google Scholar: [Google Scholar Search](#)

**39. Wilson S, Qi J, Filipp F V. Refinement of the androgen response element based on ChIP-Seq in androgen-insensitive and androgen-responsive prostate cancer cell lines. Sci Rep [Internet]. Nature Publishing Group; 2016;6:32611. Available from: <https://www.nature.com/articles/srep32611>**

Pubmed: [Author and Title](#)

Google Scholar: [Google Scholar Search](#)

**40. Pinskaya M, Saci Z, Gallopin M, Gabriel M, Nguyen HT, Firlej V, et al. Reference-free transcriptome exploration reveals novel RNAs for prostate cancer diagnosis. Life Sci Alliance. 2019;2.**

Pubmed: [Author and Title](#)

Google Scholar: [Google Scholar Search](#)

**41. Chen S, Huang V, Xu X, Livingstone J, Soares F, Jeon J, et al. Widespread and Functional RNA Circularization in Localized Prostate Cancer. Cell. 2019;176:831-843.e22.**

Pubmed: [Author and Title](#)

Google Scholar: [Google Scholar Search](#)

**42. Cejas P, Xie Y, Font-Tello A, Lim K, Syamala S, Qiu X, et al. Subtype heterogeneity and epigenetic convergence in neuroendocrine prostate cancer. Nat Commun. Nature Research; 2021;12.**

Pubmed: [Author and Title](#)

Google Scholar: [Google Scholar Search](#)



43. Imbeault M, Helleboid PY, Trono D. KRAB zinc-finger proteins contribute to the evolution of gene regulatory networks. *Nature*. Nature Publishing Group; 2017;543:550-4.  
Pubmed: [Author and Title](#)  
Google Scholar: [Google Scholar Search](#)
44. Frietze S, Lan X, Jin VX, Farnham PJ. Genomic targets of the KRAB and SCAN domain- containing zinc finger protein 263. *J Biol Chem* [Internet]. 2010;285:1393-403. Available from: <http://www.ncbi.nlm.nih.gov/pubmed/19887448>  
Pubmed: [Author and Title](#)  
Google Scholar: [Google Scholar Search](#)
45. Pope BD, Ryba T, Dileep V, Yue F, Wu W, Denas O, et al. Topologically associating domains are stable units of replication-timing regulation. *Nature* [Internet]. *Nature*; 2014 [cited 2023 Mar 27];515:402-5. Available from: <https://pubmed.ncbi.nlm.nih.gov/25409831/>
46. Barfeld SJ, Urbanucci A, Itkonen HM, Fazli L, Hicks JL, Thiede B, et al. c-Myc Antagonises the Transcriptional Activity of the Androgen Receptor in Prostate Cancer Affecting Key Gene Networks. *EBioMedicine* [Internet]. *EBioMedicine*; 2017 [cited 2023 Mar 27];18:83-93. Available from: <https://pubmed.ncbi.nlm.nih.gov/28412251/>
47. See YX, Chen K, Fullwood MJ. MYC overexpression leads to increased chromatin interactions at super-enhancers and MYC binding sites. *Genome Res* [Internet]. *Genome Res*; 2022 [cited 2023 Mar 27];32:629-42. Available from: <https://pubmed.ncbi.nlm.nih.gov/35115371/>
48. Guo H, Wu Y, Nouri M, Spisak S, Russo JW, Sowalsky AG, et al. Androgen receptor and MYC equilibration centralizes on developmental super-enhancer. *Nat Commun* [Internet]. *Nat Commun*; 2021 [cited 2023 Mar 27];12. Available from: <https://pubmed.ncbi.nlm.nih.gov/34911936/>
49. Oki S, Ohta T, Shioi G, Hatanaka H, Ogasawara O, Okuda Y, et al. ChIP-Atlas: a data-mining suite powered by full integration of public ChIP-seq data. *EMBO Rep*. 2018;19.  
Pubmed: [Author and Title](#)  
Google Scholar: [Google Scholar Search](#)
50. Urbanucci A, Barfeld SJ, Kytola V, Itkonen HM, Coleman IM, Vodak D, et al. Androgen Receptor Deregulation Drives Bromodomain-Mediated Chromatin Alterations in Prostate Cancer. *Cell Rep*. Elsevier B.V.; 2017;19:2045-59.  
Pubmed: [Author and Title](#)  
Google Scholar: [Google Scholar Search](#)
51. Lundberg A, Zhang M, Aggarwal R, Li H, Zhang L, Foye A, et al. The genomic and epigenomic landscape of double-negative metastatic prostate cancer. *Cancer Res*. 2023;  
Pubmed: [Author and Title](#)  
Google Scholar: [Google Scholar Search](#)
52. Meyer RC, Giddens MM, Schaefer SA, Hall RA. GPR37 and GPR37L1 are receptors for the neuroprotective and glioprotective factors prosaptide and prosaposin. *Proc Natl Acad Sci U S A* [Internet]. *Proc Natl Acad Sci U S A*; 2013 [cited 2023 Apr 6];110:9529-34. Available from: <https://pubmed.ncbi.nlm.nih.gov/23690594/>
53. Vierstra J, Stamatoyannopoulos JA. Genomic footprinting. *Nat Methods* [Internet]. Nature Publishing Group; 2016;13:213-21. Available from: <http://www.ncbi.nlm.nih.gov/pubmed/26914205>  
Pubmed: [Author and Title](#)  
Google Scholar: [Google Scholar Search](#)
54. Castro-Mondragon JA, Riudavets-Puig R, Rauluseviciute I, Berhanu Lemma R, Turchi L, Blanc-Mathieu R, et al. JASPAR 2022: the 9th release of the open-access database of transcription factor binding profiles. *Nucleic Acids Res* [Internet]. *Nucleic Acids Res*; 2022 [cited 2022 Nov 29];50:D165-73. Available from: <https://pubmed.ncbi.nlm.nih.gov/34850907/>

**55. Nouruzi S, Ganguli D, Tabrizian N, Kobelev M, Sivak O, Namekawa T, et al. ASCL1 activates neuronal stem cell-like lineage programming through remodeling of the chromatin landscape in prostate cancer. Nat Commun. Nature Research; 2022;13.**

Pubmed: [Author and Title](#)

Google Scholar: [Google Scholar Search](#)

**56. Bishop JL, Thaper D, Vahid S, Davies A, Ketola K, Kuruma H, et al. The master neural transcription factor BRN2 is an androgen receptor-suppressed driver of neuroendocrine differentiation in prostate cancer. Cancer Discov. American Association for Cancer Research Inc.; 2017;7:54-71.**

Pubmed: [Author and Title](#)

Google Scholar: [Google Scholar Search](#)

**57. FitsGerald PC, Shlyakhtenko A, Mir AA, Vinson C. Clustering of DNA sequences in human promoters. Genome Res [Internet]. Genome Res; 2004 [cited 2023 Mar 21];14:1562-74. Available from: <https://pubmed.ncbi.nlm.nih.gov/15256515/>**

**58. Sahu B, Laakso M, Ovaska K, Mirtti T, Lundin J, Rannikko A, et al. Dual role of FoxA1 in androgen receptor binding to chromatin, androgen signalling and prostate cancer. EMBO J. 2011;30:3962-76.**

Pubmed: [Author and Title](#)

Google Scholar: [Google Scholar Search](#)

**59. Grasso CS, Wu YM, Robinson DR, Cao X, Dhanasekaran SM, Khan AP, et al. The mutational landscape of lethal castration-resistant prostate cancer. Nature. 2012;487:239-43.**

Pubmed: [Author and Title](#)

Google Scholar: [Google Scholar Search](#)

**60. Bery F, Cancel M, Gueguinou M, Potier-Cartereau M, Vandier C, Chantome A, et al. Zeb1 and SK3 Channel Are Up-Regulated in Castration-Resistant Prostate Cancer and Promote Neuroendocrine Differentiation. Cancers (Basel) [Internet]. Cancers (Basel); 2021 [cited 2023 Mar**

**22];13. Available from: <https://pubmed.ncbi.nlm.nih.gov/34204608/>**

**61. Lee GT, Rosenfeld JA, Kim WT, Kwon YS, Palapattu G, Mehra R, et al. TCF4 induces enzalutamide resistance via neuroendocrine differentiation in prostate cancer. PLoS One [Internet]. PLoS One; 2019 [cited 2023 Mar 22];14. Available from: <https://pubmed.ncbi.nlm.nih.gov/31536510/>**

**62. Cmero M, Kurganovs NJ, Stuchbery R, McCoy P, Grima C, Ngyuen A, et al. Loss of SNAI2 in Prostate Cancer Correlates With Clinical Response to Androgen Deprivation Therapy. JCO Precis Oncol [Internet]. JCO Precis Oncol; 2021 [cited 2023 Mar 22];5:1048-59. Available from: <https://pubmed.ncbi.nlm.nih.gov/34322653/>**

**63. Zhao Y, Vartak S v., Conte A, Wang X, Garcia DA, Stevens E, et al. "Stripe" transcription factors provide accessibility to co-binding partners in mammalian genomes. Mol Cell. Cell Press; 2022;82:3398-3411.e11.**

Pubmed: [Author and Title](#)

Google Scholar: [Google Scholar Search](#)

**64. Che M, Chaturvedi A, Munro SA, Pitzen SP, Ling A, Zhang W, et al. Opposing transcriptional programs of KLF5 and AR emerge during therapy for advanced prostate cancer. Nat Commun [Internet]. Nature Research; 2021;12:6377. Available from: <http://www.ncbi.nlm.nih.gov/pubmed/34737261>**

Pubmed: [Author and Title](#)

Google Scholar: [Google Scholar Search](#)

**65. Cui J, Liu J, Fan L, Zhu Y, Zhou B, Wang Y, et al. A zinc finger family protein, ZNF263, promotes hepatocellular carcinoma resistance to apoptosis via activation of ER stress-dependent autophagy. Transl Oncol [Internet]. Neoplasia Press, Inc.; 2020;13:100851. Available from: <http://www.ncbi.nlm.nih.gov/pubmed/32898766>**

Pubmed: [Author and Title](#)

Google Scholar: [Google Scholar Search](#)

**66. Yu Z, Feng J, Wang W, Deng Z, Zhang Y, Xiao L, et al. The EGFR-ZNF263 signaling axis silences SIX3 in glioblastoma epigenetically. Oncogene [Internet]. Springer Nature; 2020;39:3163-78. Available from:**



<http://www.ncbi.nlm.nih.gov/pubmed/32051553>

Pubmed: [Author and Title](#)

Google Scholar: [Google Scholar Search](#)

**67. Thurman RE, Rynes E, Humbert R, Vierstra J, Maurano MT, Haugen E, et al. The accessible chromatin landscape of the human genome. Nature [Internet]. 2012;489:75-82. Available from: <http://www.ncbi.nlm.nih.gov/pubmed/22955617>**

Pubmed: [Author and Title](#)

Google Scholar: [Google Scholar Search](#)

**68. Samarasinghe KTG, Jaime-Figueroa S, Burgess M, Nalawansa DA, Dai K, Hu Z, et al. Targeted degradation of transcription factors by TRAFACs: TRANscription Factor TARgeting Chimeras. Cell Chem Biol. Elsevier Ltd; 2021;28:648-661.e5.**

Pubmed: [Author and Title](#)

Google Scholar: [Google Scholar Search](#)

**69. Henley MJ, Koehler AN. Advances in targeting 'undruggable' transcription factors with small molecules. Nat Rev Drug Discov. Nature Research; 2021. page 669-88.**